

FACULTY OF PHYSICS AND ASTRONOMY  
UNIVERSITY OF HEIDELBERG

Diploma thesis  
in Physics

submitted by  
Christian H. Schunck  
born in  
Hagen, Westf.

2002



STUDY OF AN ULTRACOLD CLOUD OF FERMIONIC  ${}^6\text{Li}$   
ATOMS NEAR A FESHBACH RESONANCE

This diploma thesis has been carried out by Christian Schunck  
at the Physiklisches Institut  
under the supervision of  
Prof. Dr. Jörg Schmiedmayer

# UNTERSUCHUNG EINES ULTRAKALTEN GASES FERMIONISCHER ${}^6\text{Li}$ ATOME IN DER NÄHE EINER FESHBACH-RESONANZ

In dieser Diplomarbeit wird ein ultrakaltes Fermi-Gas aus  ${}^6\text{Li}$  Atomen untersucht. Auf der Suche nach neuen makroskopischen Quantenphänomenen in fermionischen Gasen, insbesondere eines Bardeen-Cooper-Schrieffer- (BCS) Übergangs, gilt das Interesse der Erzeugung starker und attraktiver Wechselwirkungen via Feshbach-Resonanzen. In den durchgeführten Experimenten wurden solche Resonanzen über inelastische Verluste beobachtet. Dafür wurden  ${}^6\text{Li}$ -Atome in einer Magnetfalle mit bosonischen  ${}^{23}\text{Na}$ -Atomen sympathetisch in das quantenentartete Regime gekühlt. Dann wurden die  ${}^6\text{Li}$ -Atome in eine optische Falle geladen, dort in unterschiedlichen Spinmischungen präpariert und Magnetfeldern bis zu 900 G ausgesetzt. Die Spinmischung aus Atomen in den beiden niedrigsten Hyperfeinzuständen zerfiel resonant für Magnetfelder von 550 und 680 G. Dies ist konsistent mit den vorhergesagten elastischen Feshbach-Resonanzen für s-Wellen-Stöße. Die beobachtete Lebensdauer betrug mehrere hundert Millisekunden und ist lang im Vergleich zu der erwarteten Zeitdauer für Cooper-Paarbildung und damit eines BCS-Phasenübergangs. Die Magnetfelder wurden mit den Spulen einer "Cloverleaf"-Magnetfalle produziert. Einschränkungen durch eine ungünstige Spulenkonfiguration wurden durch den Bau einer neuen Magnetfalle behoben, die hohe, stabile und homogene Magnetfelder sowie einen stärkeren Einschluß der Atome bietet.

## STUDY OF AN ULTRACOLD CLOUD OF FERMIONIC ${}^6\text{Li}$ ATOMS NEAR A FESHBACH RESONANCE

This thesis describes the experimental study of an ultracold  ${}^6\text{Li}$  Fermi gas. The search for new macroscopic quantum phenomena in fermionic gases, in particular a Bardeen-Cooper-Schrieffer (BCS) transition, requires the achievement of strong and attractive interactions. These interactions can be tuned by Feshbach resonances. In the performed experiments, Feshbach resonances were observed via inelastic losses in the  ${}^6\text{Li}$  cloud. The quantum degenerate sample of  ${}^6\text{Li}$  was produced in a magnetic trap via sympathetic cooling with a bosonic  ${}^{23}\text{Na}$  reservoir. The experiment involved transferring the  ${}^6\text{Li}$  atoms into an optical trap and required controlling the spin composition of the optically trapped sample. The atoms were then subjected to magnetic fields up to 900 G. The spin mixture of the two lowest hyperfine states showed two decay resonances at 550 and 680 G, consistent with the predicted Feshbach resonances for elastic s-wave collisions. The observed lifetimes of several hundred milliseconds are long compared to the expected time for Cooper pair formation and a BCS transition. Initially the magnetic bias fields were produced with the coils of a cloverleaf magnetic trap. Inherent limitations of this trap were overcome by manufacturing a modified trap that provides high and homogeneous bias fields as well as an improved confinement.

TAT  
(Goethe)

Ich weiß nicht womit ich es sagen soll,  
denn mein Wort ist immer noch nicht  
geformt

*Juan Antonio Jiminez*



# Contents

|          |   |           |
|----------|---|-----------|
| <b>1</b> | <b>Introduction</b>   | <b>3</b>  |
| 1.1      | Ultracold fermionic gases . . . . .   | 3         |
| 1.2      | This thesis . . . . .   | 4         |
| <b>2</b> | <b>Production of a degenerate mixture of <math>^6\text{Li}</math> and <math>^{23}\text{Na}</math></b> | <b>7</b>  |
| 2.1      | Loading of the double species Magneto-Optical Trap . . . . .  | 7         |
| 2.2      | Magnetic trapping . . . . .   | 8         |
| 2.3      | Sympathetic cooling of $^6\text{Li}$ with $^{23}\text{Na}$ . . . . .                                  | 11        |
| <b>3</b> | <b>The Feshbach Experiment</b>  | <b>15</b> |
| 3.1      | Feshbach Resonances . . . . .   | 15        |
| 3.2      | Preparation of the spin mixture . . . . .   | 20        |
| 3.3      | Production of high magnetic fields . . . . .  | 23        |
| 3.4      | Magnetic field dependent decay of the $^6\text{Li}$ cloud . . . . .                                   | 28        |
| <b>4</b> | <b>The new magnetic trap</b>  | <b>33</b> |
| 4.1      | The Design of the new trap . . . . .  | 33        |
| 4.2      | Selection of materials and construction . . . . .   | 35        |
| 4.3      | Flow and temperature interlock . . . . .  | 41        |
| 4.4      | Installation and operation of the new trap . . . . .  | 42        |
| <b>5</b> | <b>Conclusion and Outlook</b>   | <b>45</b> |
| <b>A</b> | <b>Calculation of the magnetic fields</b>   | <b>47</b> |
| A.1      | Circular coils . . . . .  | 47        |
| A.2      | Cloverleaf coils . . . . .  | 47        |
| A.3      | Parameters for the calculation and results . . . . .  | 49        |
| <b>B</b> | <b>Electric connections of the trap</b>   | <b>53</b> |
| <b>C</b> | <b>Water distribution panel</b>   | <b>59</b> |





# Chapter 1

## Introduction

### 1.1 Ultracold fermionic gases

The achievement of Bose-Einstein condensation (BEC) in trapped alkali atoms in 1995 [1] opened a new and fast expanding area of research in atomic physics. Among their many interesting properties, Bose-Einstein condensates are ideally suited for the study of many body physics, despite their extreme diluteness. Since the condensates are only weakly interacting, their collective properties are not blurred by strong interactions as in condensed matter systems. This has allowed detailed studies of their superfluid properties and quantum phase transitions [2]. Furthermore it has been shown that the inter-particle interactions in ultracold gases can be tuned by magnetic fields [3]. This provides an important tool to control and fundamentally change the properties of these atomic systems.

This research motivated the quest for finding macroscopic quantum effects in trapped, ultracold, degenerate Fermi gases. Specifically, a superfluid Bardeen-Cooper-Schrieffer (BCS) transition is predicted to be within experimental reach. Compared to their bosonic counterparts, quantum degenerate Fermi gases have fundamentally different properties. At a critical temperature,  $T_C$ , bosons undergo a phase transition in which they accumulate in the ground state of the system and condense. Due to the Pauli exclusion principle, identical fermions have to occupy orthogonal quantum states and form a Fermi Sea. In the zero temperature limit the energy of the highest occupied state is called the Fermi Energy  $E_F$ . The corresponding Fermi temperature is  $T_F = E_F/(k_B)$ . The critical temperature  $T_C$  for BEC, and the Fermi temperature  $T_F$  mark the onset of quantum degeneracy in the atomic clouds and are of the same order of magnitude. At these temperatures, the thermal deBroglie wavelength of the atoms becomes comparable to interatomic distances. The wavefunctions of the particles start to overlap and quantum statistics becomes important.

Since at the temperatures attainable by laser cooling quantum statistics is not important, all laser cooling techniques can be applied to fermionic atoms. But the final cooling stage of evaporative cooling, usually in a magnetic trap, fails for a cold gas

of identical fermions. Evaporative cooling is based on the removal of the most energetic atoms from the gas and subsequent rethermalization of the remaining atoms by elastic collisions. At low temperatures, p-wave scattering is suppressed due to the centrifugal barrier and only s-wave scattering is energetically possible. However, s-wave scattering is forbidden for identical fermions by symmetry. Thus, evaporative cooling cannot be applied on a single-component Fermi gas.

This problem has been solved by using a mixture of distinguishable atoms for *sympathetic* cooling. Then, s-wave scattering is allowed via inter-species collisions. The mixtures can consist of different spin states of the same fermionic atom, different atomic isotopes or different elements. However, there are more fundamental cooling limits. If most of the states in the Fermi system are already occupied, the phase space for scattering to lower energy states is limited (Pauli blocking) and the efficiency of the cooling drops. Furthermore, inelastic losses can create holes in the Fermi sea and the following relaxation of atoms into these holes can lead to heating [36].

Quantum degeneracy in a fermionic cloud was first achieved in a mixture of two different spin states of  $^{40}\text{K}$  in the group of D. Jin at JILA [4, 5]. In experiments that involve mixtures of fermions in different spin states, both components of the system are evaporated to achieve efficient cooling. However, if fermions are sympathetically cooled in a large bosonic “refrigerator”, only the bosonic atoms need to be evaporated. Furthermore, the bosonic component of the mixture does not suffer from the limited phase space due to already occupied states. Finally, boson-fermion mixtures allow for studies of the interaction between these different systems in the quantum degenerate regime. R. Hulet at Rice and C. Salomon at ENS in Paris have achieved quantum degeneracy in a mixture of bosonic  $^7\text{Li}$  and fermionic  $^6\text{Li}$  [12, 13]. These experiments, however, are limited due to the instability of the  $^7\text{Li}$  condensate and unfavorable scattering properties [14, 13].

Simultaneous quantum degeneracy in a Bose-Fermi mixture of different atomic species has first been achieved in W. Ketterle’s group at MIT [15]. A large  $^{23}\text{Na}$  cloud is used to sympathetically cool  $^6\text{Li}$ . In M. Inguscio’s group at Florence,  $^{40}\text{K}$  is cooled into degeneracy with  $^{87}\text{Rb}$  [21, 22]. J. Thomas at Duke achieves quantum degeneracy by evaporating a spin mixture of  $^6\text{Li}$  in an all-optical trap [18]. The above mentioned experiments reach temperatures between 0.2 and 0.5  $T_F$ .

The first experiments performed with fermionic gases clearly showed the expected decrease of the p-wave scattering cross section with decreasing temperatures [5] and revealed the effects of Pauli blocking and Fermi pressure [12, 7]. Since then Fermi gases have been studied in the hydrodynamic regime and effects of quantum degeneracy have been observed in a reduced damping time of collective oscillations [8, 9]. In view of the challenging goal to achieve a superfluid BCS-like phase transition, current experimental efforts are focusing on creating large and attractive interactions in the degenerate fermionic cloud. Such attractive interactions between fermionic atoms in two different spin states induce Cooper pairing at a critical temperature that is given by [32]:

$$T_C \simeq \frac{E_F}{k_B} \exp\left(-\frac{\pi}{2k_F|a|}\right) \quad (1.1)$$

where  $E_F$  and  $k_F$  are the Fermi energy and momentum respectively and  $|a|$  is the value of the negative scattering length. As can be seen from equation 1.1, the transition temperature depends crucially on the value of  $a$ .  $^6\text{Li}$  as well as  $^{40}\text{K}$  spin mixtures that are stable against spin exchange losses, exhibit a so called Feshbach resonance. In the vicinity of such a resonance,  $|a|$  is tunable to extremely large negative values by externally applied magnetic fields. This can increase the BCS transition temperature  $T_C$  to temperatures very close to  $T_F$ . In comparison, typical values of  $T_C/T_F$  in high-temperature superconductors are one to two orders of magnitude smaller. Therefore a BCS transition in an atomic cloud would allow the study of BCS physics in a new regime.

Feshbach resonances in  $^{40}\text{K}$  have been studied in D. Jin's group [9, 10]. This thesis describes an experiment with the goal of observing a signature of the Feshbach resonance predicted for  $^6\text{Li}$ .

## 1.2 This thesis

We study the magnetic field dependence of the inelastic decay of an ultracold cloud of fermionic  $^6\text{Li}$  near a Feshbach resonance. The quantum degenerate sample of  $^6\text{Li}$  is produced in a magnetic trap via sympathetic cooling with a  $^{23}\text{Na}$  condensate as reported in [15].

The experiment involved the transfer of the  $^6\text{Li}$  atoms into an optical trap and required the control of the spin composition of the optically trapped sample. This cloud was then subjected to magnetic fields up to 900 G. Initially high magnetic bias fields were produced with the coils of our cloverleaf magnetic trap [42]. To overcome inherent limitations due its coil configuration, a modified trap has been built. It provides high and stable bias fields with negligible curvature as well as an improved confinement.

In the second chapter, a review on the sympathetic cooling of  $^6\text{Li}$  with  $^{23}\text{Na}$  is given. Special attention is paid to magnetic trapping and the production of the associated magnetic fields. The third chapter is based on the research reported in [16] and presents a short overview of scattering theory and scattering resonances, followed by a detailed description of the performed decay experiment. In the fourth chapter, I summarize all aspects of the design and features of the new magnetic trap. I close with an outlook on further steps towards the achievement of a BCS transition.



# Chapter 2

## Production of a degenerate mixture of $^6\text{Li}$ and $^{23}\text{Na}$

In this chapter, the sympathetic cooling of  $^6\text{Li}$  with  $^{23}\text{Na}$  is discussed. Special attention is paid to aspects related to magnetic trapping.

### 2.1 Loading of the double species Magneto-Optical Trap

Obtaining a double species magneto-optical trap (MOT) of  $^6\text{Li}$  and  $^{23}\text{Na}$  was the first crucial step towards quantum degenerate  $^6\text{Li}$  and involved the development of a laser system for lithium as well as the installment of a double species oven on the existing  $^{23}\text{Na}$  BEC machine. A detailed description of the new laser system and the overlapped  $^6\text{Li}$  and  $^{23}\text{Na}$  MOT is given in [46] and [47].

The  $^6\text{Li}$  and  $^{23}\text{Na}$  vapors are produced in a double species oven, that delivers a collinear beam of  $^6\text{Li}$  and  $^{23}\text{Na}$  atoms at thermal velocities of several 100m/s. In the first step of the cooling process, the atoms are decelerated in a Zeeman slower [49]. Due to the Doppler shift, atoms in a narrow velocity range absorb photons from a counter-propagating laser beam, red detuned to the atomic resonance. Since the subsequent spontaneous emission of photons is isotropic, the atoms experience a net momentum transfer in the direction opposite to their motion and are slowed down. In order to keep them in resonance with the laser light, an inhomogeneous magnetic field is applied along the direction of propagation. This shifts the atomic energy levels and compensates for the changing Doppler shift during the deceleration. The atoms leave the Zeeman slower with speeds on the order of 10m/s and can be captured in a MOT.

A MOT is based on the same ideas used for Zeeman slowing, but applied in three dimensions. In addition to cooling, this confines the atoms in space. In a MOT the atoms are irradiated by six red detuned laser beams of different polarizations. A spherical quadrupole magnetic field

$$\vec{B}_{MOT} = \frac{B'}{2} \begin{pmatrix} x \\ y \\ -2z \end{pmatrix} \quad (2.1)$$

provides the magnetic field gradients. This field can easily be produced by circular electromagnets in an "anti-Helmholtz" configuration, i.e. with currents running in opposite directions (see figure 2-1(b)). Its zero-field point determines the center of the trap, where the atoms are compressed due to the light pressure of the trap laser beams. Atoms leaving the trap center experience an increasing magnetic field that lifts the degeneracy of their Zeeman levels. This shifts the atoms closer to resonance with the laser beam opposing their motion. Therefore they will preferably scatter photons from the counter-propagating beam which results in a restoring force towards the trap center. A one dimensional illustration is shown in figure 2-1(a).

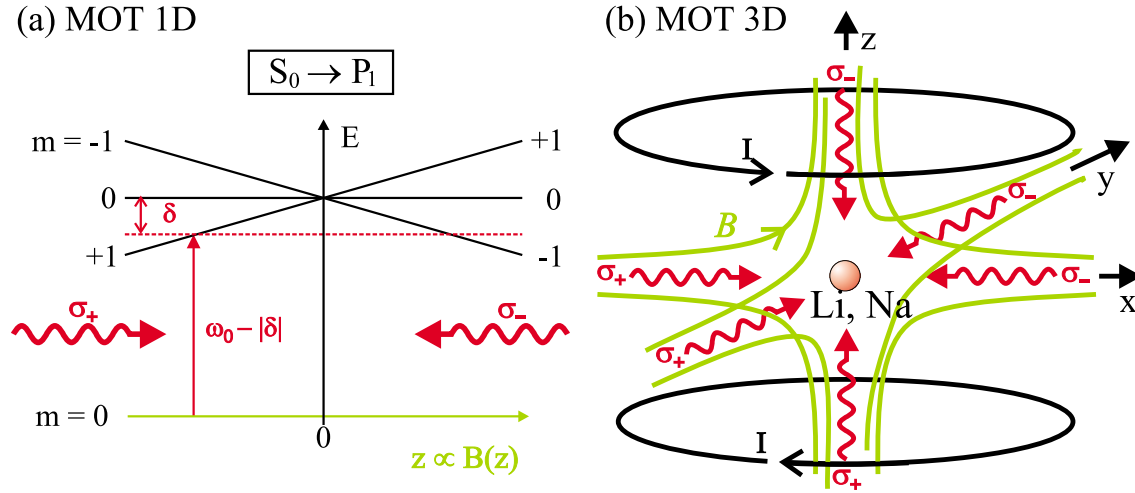


**Figure 2-1:** The Magneto-Optical-Trap for a hypothetical atom with  $S=I=0$  in one and three dimensions. (a) The light for the  $S_0 \rightarrow P_1$  transition is red detuned to the atomic resonance by  $\delta$ . Consider an atom moving to the right. The magnetic field shifts the  $m = -1$  level of the excited state into resonance with the  $\sigma_-$  polarized beam while the  $m = +1$  level is shifted out of resonance with the  $\sigma_+$  polarized beam.

The temperature achievable in a MOT is limited by heating caused by spontaneous emission. The cooling limit is given by the Doppler temperature  $T_D = \frac{\hbar\Gamma}{2k_B}$  proportional to the natural linewidth  $\Gamma$ . The Doppler temperatures for  $^6\text{Li}$  and  $^{23}\text{Na}$  are  $140 \mu\text{K}$  and  $240 \mu\text{K}$  respectively. We achieve a  $^6\text{Li}$  MOT temperature of  $700 \mu\text{K}$  for  $5 \cdot 10^6$  atoms at densities of  $3 \cdot 10^9/\text{cm}^3$ .

However, sub-Doppler temperatures can be realized with a laser cooling technique known as polarization gradient cooling, or Sisyphus cooling [55, 51, 52]. After switching off the MOT fields, we use polarization gradient cooling for a few ms to cool  $^{23}\text{Na}$  to a temperature of  $100 \mu\text{K}$ . We have not implemented sub-Doppler cooling for lithium, since it was found to be inefficient [48]. The next step in the cooling process

is to load the precooled atoms into the conservative potential of a magnetic trap, and apply evaporative cooling.

## 2.2 Magnetic trapping

Alkali atoms have one unpaired electron, which apart from a small contribution of the nucleus, gives rise to their magnetic moment  $\vec{\mu}$  on the order of one Bohr magneton  $\mu_B$  in the electronic ground state. The interaction energy  $U$  of an atom in an external magnetic field  $\vec{B}(\vec{r})$  is given by

$$U = -\vec{\mu} \cdot \vec{B}(\vec{r}) \quad (2.2)$$

At low magnetic fields, the total angular momentum  $\vec{J}$  of the electron and the spin  $\vec{I}$  of the nucleus are tightly coupled by the hyperfine interaction. Then  $\vec{\mu}$  is proportional to  $\vec{F} = (\vec{I} + \vec{J})$ , i.e.  $\vec{\mu} = -g_F \mu_B \vec{F}$  and equation 2.2 can be simplified to  $U = g_F m_F \mu_B |\vec{B}(\vec{r})|$ . In the ground state of all alkali atoms,  $g_F$  is given by  $g_F = I \pm 1/2 = \pm 1/(I + 1/2)$ . The sign of  $g_F m_F$  determines whether an atom in state  $|F, m_F\rangle$  minimizes its energy by seeking a magnetic field minimum or maximum. The states  $|F, m_F\rangle$  are called low and high field seekers accordingly. Since it is not possible to create a local maximum of a static magnetic field in free space [57], only low field seeking states can be trapped in a DC magnetic trap.

With increasing magnetic field the nuclear and electron spin start to decouple and eventually precess separately about the external magnetic field. This gives rise to a low field quadratic Zeeman shift, as described by the Breit-Rabi formula [61]. Due to the quadratic Zeeman effect, low field seeking states can eventually become high field seeking (and vice versa) with increasing fields. In  $^6\text{Li}$  this is the case for the  $|1/2, -1/2\rangle$  state (see figure 2-3): it becomes high field seeking already at moderate magnetic fields of 27 G.

The quantization axis for the atomic magnetic moment is given by the direction of the local magnetic field. In the frame of an atom moving in a magnetic trap, the field is time dependent and varies in direction and magnitude. If the trap frequencies are significantly smaller than the Larmor frequency  $\omega_L = \mu_0 |\vec{B}_0|/\hbar$ , the magnetic moment of the atom will follow the field adiabatically. But if the minimum of the magnetic trap is close to zero (which is for example the case for the spherical quadrupole field of the MOT), spin flips to untrapped states are possible - so called “Majorana flops” Therefore a magnetic trap has to provide at least harmonic confinement, which leaves the possibility for a finite offset field.

### 2.2.1 Ioffe-Pritchard trap

#### The trapping potential

The strongest magnetic confinement at a finite offset field is provided by Ioffe-Pritchard traps [58, 56]. The trapping potential has cylindrical symmetry. With the trap center chosen as the origin and the z-axis as the symmetry axis, the field inside the coil ensemble can be described by the following two components:

- A two dimensional quadrupole field in the radial plane providing a radial gradient  $B'$ :

$$\vec{B}_G(x, y, z) = B' \begin{pmatrix} x \\ -y \\ 0 \end{pmatrix} \quad (2.3)$$

- A harmonic potential  $B = B''z^2 + B_0$ , with an axial curvature of  $B''$  and a finite, uniform bias field  $B_0$  along the symmetry axis.  $\nabla \cdot \vec{B} = 0$  and  $\nabla \times \vec{B} = 0$  together with the axial symmetry require this potential to be accompanied by a radial field of

$$-\frac{B''z}{2} \begin{pmatrix} x \\ y \\ 0 \end{pmatrix} \quad (2.4)$$

and an additional contribution in the axial direction of  $-1/4B''(x^2 + y^2)$ , respectively.

Therefore the total field configuration is given by:

$$\vec{B} = B_0 \begin{pmatrix} 0 \\ 0 \\ 1 \end{pmatrix} + B' \begin{pmatrix} x \\ -y \\ 0 \end{pmatrix} + \frac{B''}{2} \begin{pmatrix} -xz \\ -yz \\ z^2 - \frac{1}{2}(x^2 + y^2) \end{pmatrix} \quad (2.5)$$

and the field strength in the trap can be calculated to be:

$$|\vec{B}| = \sqrt{\left[ B_0^2 + B_0 B'' z^2 + \frac{B''^2 z^4}{4} \right] + \left[ \left( B'^2 - \frac{B'' B_0}{2} \right) r^2 + \frac{B''^2 r^4}{16} \right] + B' B'' z (y^2 - x^2)} \quad (2.6)$$

with  $r = \sqrt{x^2 + y^2}$ .

Close to the trap center (i.e. for  $\vec{B}(x, y, z) - B_0/b_0 \ll 1$ ), this yields a harmonic potential:

$$U(r, z) = |\mu| \left( B_0 + \frac{1}{2} \left( \frac{B'^2}{B_0} - \frac{B''}{2} \right) \rho^2 + \frac{1}{2} B'' z^2 \right) \quad (2.7)$$



A low temperature cloud with ( $k_B T < |\mu| B_0$ ) experiences this harmonic potential with an axial curvature  $B''$  and a radial curvature of

$$B''_r = \frac{B'^2}{B_0} - \frac{B''}{2} \quad (2.8)$$

which yields the trap frequencies:

$$\omega_{z,r} = \sqrt{\frac{\mu_B g_F m_F}{m} B''_{z,r}} \quad (2.9)$$

In equation 2.8 the second term is usually much smaller than the first and can often be neglected. The geometric mean of the trapping frequencies is given by

$$\bar{\omega} = (\omega_x \omega_y \omega_z)^{1/3} = (\omega_r^2 \omega_z)^{1/3} \sim \left( \frac{B'' B'^4}{B_0^2} \right)^{1/6} \quad (2.10)$$

$\bar{\omega}$  is proportional to the BEC transition temperature of

$$T_c = \frac{\hbar \bar{\omega}}{k_B} \left( \frac{N}{1.202} \right)^{1/3} \quad (2.11)$$

and  $\bar{\omega}^2$  to the rate of elastic collisions in the purely harmonic trap, which determines the efficiency of evaporation.

### Realization of a Ioffe-Pritchard trap

The winding pattern of a Ioffe-Pritchard trap is not unique. A cloverleaf trap is used on our experiment [42]. The radial gradient  $B'$  is produced by eight cloverleaf coils (see figure 2-2).

The axial curvature is generated by a pair of circular "curvature" coils with currents running in the same direction (Helmholtz configuration). Apart from the axial curvature  $B''$  they also generate an axial offset field  $B_0$ . The distance  $r$  between the coils and the trap center is usually a bit larger than a centimeter and since  $B'' \sim B_{\text{curv}}/r^2$ , a curvature of 1 G/cm<sup>2</sup> gives an offset field of a few G. Reasonable axial trap frequencies allowing for efficient evaporative cooling are about  $\omega_z = 2\pi \cdot 20$  Hz. For a typical alkali atom with a mass on the order of  $10/(10^3 N_A)$  kg and a magnetic moment of about one  $\mu_B = 1.4$  MHz/G, this requires an axial curvature  $B'' = \omega_z^2/(10^2 N_A \mu_B)$  of about 30 G/cm<sup>2</sup>, accompanied by offset fields  $B_0$  up to 100 G. According to equation 2.10 such an offset field would reduce  $\bar{\omega}$  and make efficient evaporation impossible. Therefore  $B_0$  has to be cancelled, just leaving a bias field high enough to avoid Majorana losses (which is about 1 G). This is done by a pair of "anti-bias" coils. These coils also operate in a Helmholtz configuration but with a current running in the direction opposite to the one in the curvature coils. Because of their large radius, the antibias coils can generate the required anti-bias field without producing a significant curvature.

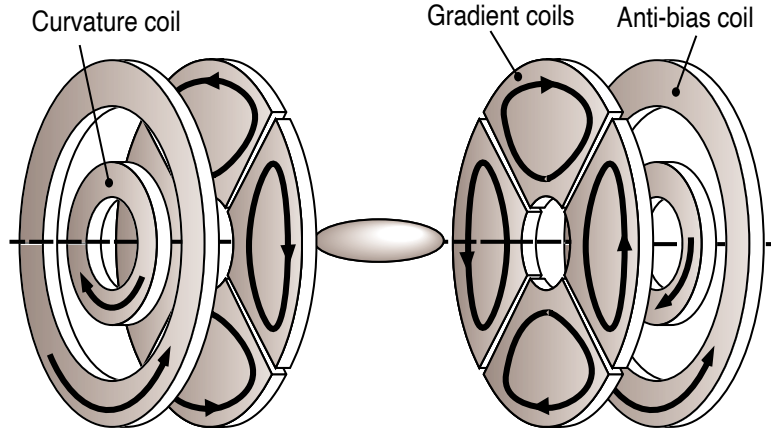


**Figure 2-2:** Four cloverleaf coils on each side of the trap and in the planes close to the atoms provide the radial gradient. A small pair of curvature coils generating the axial curvature is surrounded by a larger pair of antibias coils, which compensates for the bias field produced by the curvature coils. Curvature and antibias coils are located in the two planes further away from the atoms. The arrows indicate the direction of the currents. Figure adapted from [44].

Since the described adjustment of  $B_0$  relies on the subtraction of two large numbers (about 100 G each) to give a small residual one (about 1 G), this system is very sensitive to fluctuations. A 1% change in the current through the antibias coils could already zero the bias field and one would suffer from Majorana losses. This problem is solved by connecting antibias and curvature coils in series and running the same current through all of them. However, this requires designing and building the antibias coils so carefully that they cancel the bias field of the curvature coils to exactly 1 G at a current which generates the desired curvature. Practically this is not possible and the errors can be as large as 10% of the nominal fields. Therefore a movable coil, the “trombone” coil is put in series with the curvature and antibias coils. By adjusting its distance from the trap center over a range of a few centimeters,  $B_0$  can be set to 1 G.

## 2.3 Sympathetic cooling of ${}^6\text{Li}$ with ${}^{23}\text{Na}$

Evaporative cooling is based on the removal of the “hottest” atoms from the magnetic trap and relies on the rethermalization of the remaining atoms by elastic collisions. To scatter a particle with an angular momentum on the order of  $\hbar$  at a potential of range  $r_0$ , its momentum has to be larger than  $p = \hbar/r_0$  due to the centrifugal barrier. Already at temperatures below  $100\ \mu\text{K}$ , p-wave scattering is suppressed [5, 6] and only s-wave scattering is possible. However, for spin-polarized fermions s-wave scattering is forbidden by symmetry. We solve this problem by cooling  ${}^6\text{Li}$  with a large  ${}^{23}\text{Na}$  cloud, that acts like a refrigerator. While  ${}^{23}\text{Na}$  is evaporated,  ${}^6\text{Li}$  atoms

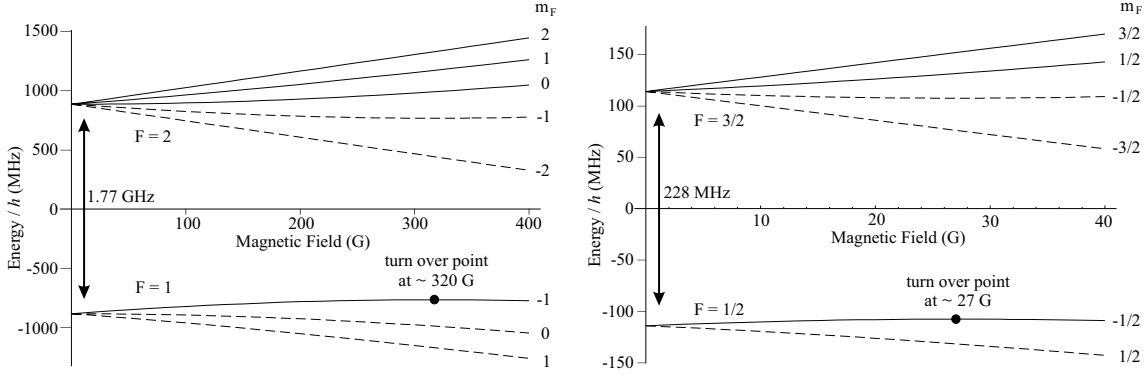


**Figure 2-3:** Zeeman splitting of the  $F=1$  and  $F=2$  hyperfine states of  ${}^{23}\text{Na}$  and the  $F=1/2$  and  $F=3/2$  hyperfine states of  ${}^6\text{Li}$ . Due to the quadratic Zeeman shift, the  $|1, -1\rangle$  state in  ${}^{23}\text{Na}$  and the  $|1/2, -1/2\rangle$  state in  ${}^6\text{Li}$  become high field seeking at 320 G and 27 G respectively.

thermalize due to elastic s-wave collisions with  ${}^{23}\text{Na}$ , and are thus sympathetically cooled.

### 2.3.1 Evaporative cooling of sodium

The  ${}^{23}\text{Na}$  BEC is produced in the  $|F, m_F\rangle = |1, -1\rangle$  lower hyperfine ground state. This state is low field seeking for magnetic fields up to 316 G. Since most sodium atoms in the (dark) MOT are in the  $F=1$  hyperfine manifold, the transfer efficiency into the magnetic trap is about 30%. To prevent losses in the phase-space density, the magnetic trap should match the size, aspect ratio and temperature of the pre-cooled cloud. Therefore we give the trap initially a roughly spherical symmetric shape by running an additional current through the curvature coils. This raises the bias field  $B_0$ , thus lowering the radial curvature. After the atoms are caught, the trap is adiabatically compressed by reducing  $B_0$  to 1G. This increases the collision rate between the atoms and is the starting point for forced radio-frequency (RF) evaporative cooling [59, 62].

The idea underlying RF forced evaporation is simple: In the magnetic trap, the potential energy of the atoms is magnetic field dependent (see figure 2-3). For the  $|1, -1\rangle$  state of  ${}^{23}\text{Na}$  the energy at a magnetic field of magnitude  $B$  is given by:

$$E = \frac{1}{2}\mu_B(B - B_0) \quad (2.12)$$

In order to remove the atoms above a certain truncation energy  $E_\tau(B_\tau)$  a RF-”knife” is applied. It drives a transition to an untrapped state so that the atoms with  $E > E_\tau$  are expelled from the trap. If the remaining atoms rethermalize by elastic collisions, cooling is achieved. We use the  $|1, -1\rangle$  to  $|2, -2\rangle$  transition at 1.77GHz for evaporative cooling. Thus a truncation energy of  $E_\tau$  corresponds to a

RF-”knife” frequency of

$$\omega_{rf} = 1.77\text{GHz} - \frac{3\mu_B}{2\hbar}B_\tau \quad (2.13)$$

By lowering the RF-knife (in our case this is done by increasing  $\omega_{rf}$ ), the temperature of the atomic cloud is reduced. For efficient, ”runaway” evaporation this RF-sweep is tweaked so that the collision rate increases during the evaporation process [62, 60].

### 2.3.2 Sympathetic Cooling of $^6\text{Li}$ in the magnetic trap

It would be favorable to have ultracold  $^6\text{Li}$  in the  $|1/2, -1/2\rangle$  hyperfine state for two reasons:

- a mixture of  $^6\text{Li}$  and  $^{23}\text{Na}$  in the  $|1/2, -1/2\rangle$  and  $|1, -1\rangle$  states respectively is stable against inelastic spin exchange collisions
- we want to study the strong interactions predicted for the  $F=1/2$  hyperfine state

However, as mentioned earlier, this state becomes high field seeking at magnetic fields above 27 G. This results in a maximum magnetic trap depths of about  $300\mu\text{K}$ . However, the temperature of the  $^6\text{Li}$  MOT is  $700\mu\text{K}$ . Therefore we trap  $^6\text{Li}$  initially in the upper hyperfine manifold.

An illustration of our sympathetic cooling procedure is given in figure 2-4.

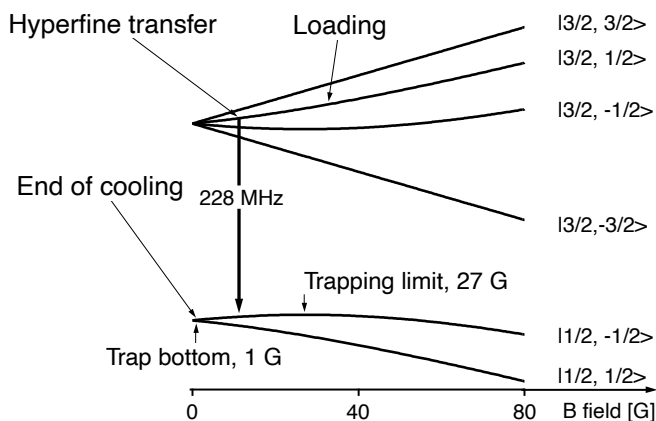


**Figure 2-4:** Sympathetic cooling scheme for  $^6\text{Li}$  with  $^{23}\text{Na}$ . Shown is the magnetic field dependence of the two ground state hyperfine levels of  $^6\text{Li}$ . Figure adapted from [15].

The  $^6\text{Li}$  atoms are pumped from the  $^6\text{Li}$  MOT into the upper hyperfine manifold and loaded together with  $^{23}\text{Na}$  into the magnetic trap. Then, the  $^{23}\text{Na}$  cloud is cooled down to  $50\mu\text{K}$  by rapid RF-forced evaporation. Because the sympathetic cooling of  $^6\text{Li}$  with  $^{23}\text{Na}$  is efficient, this can be done fast (in about 5s) and with low  $^6\text{Li}$  losses.

At this point a substantial fraction of the lithium atoms is in the  $|3/2, 1/2\rangle$  state and can be transferred to the lower hyperfine state by a single photon RF transition at 228 MHz. The remaining  ${}^6\text{Li}$  atoms in the upper state are removed by a light pulse and we resume the evaporative cooling of  ${}^{23}\text{Na}$  for about 10 s.

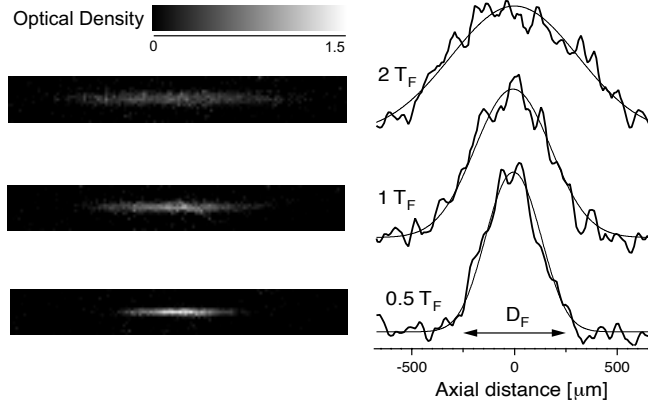


**Figure 2-5:** Absorption images and axial line density profiles for  ${}^6\text{Li}$  corresponding to temperatures of  $T/T_F = 2, 1, 0.5$ . Since only  ${}^{23}\text{Na}$  is evaporated, the total number of atoms remains constant. The shrinking of the cloud and the increase in the optical density are due to efficient cooling. Figure adapted from [15].

Figure 2-5 shows absorption images of  ${}^6\text{Li}$  in the magnetic trap as it is cooled into quantum degeneracy. The temperature is measured in units of the Fermi temperature  $T_F$ . For harmonic confinement,  $T_F$  is given by:

$$T_F = \frac{\hbar\bar{\omega}}{k_B} [6N]^{1/3} \quad (2.14)$$

with  $\bar{\omega}$  being the geometric mean of the trapping frequencies and  $N$  the atom number. The temperatures were determined by semi-classical Thomas-Fermi fits to the axial density profiles. For comparison the Fermi diameter  $D_F = \sqrt{2k_B T_F / (m\omega_z^2)}$  is plotted. It gives the minimum size the cloud would assume in the zero temperature limit: measured from the trap center,  $R_F = D_F/2$  is the largest axial distance a classical particle with an energy equal to the Fermi energy  $E_F = k_B T_F$  could reach. We reach temperatures of about 300nK, corresponding to  $T/T_F = 0.5$ .



# Chapter 3

## The Feshbach Experiment

In this chapter, the study of inelastic losses in a fermionic  ${}^6\text{Li}$  cloud in the vicinity of a Feshbach resonance is presented. In the first section, a brief overview of scattering theory and scattering resonances is given. The predicted Feshbach resonance is presented and its importance for the achievement of a BCS transition is discussed. The experiment required trapping the atoms in an optical dipole trap, controlling the different spin states in the sample and generating the necessary magnetic fields to reach the Feshbach resonance. Each of these steps will be reviewed in the second part of this chapter.

Finally we present the experimental observations and discuss the results.

### 3.1 Feshbach Resonances

#### 3.1.1 Scattering theory

We describe the scattering of two distinguishable particles in the center of mass frame. The Schrödinger equation for the scattering of a particle with reduced mass  $\mu = \frac{m_1 m_2}{m_1 + m_2}$  and energy  $E = \frac{\hbar^2 k^2}{2\mu}$  from a potential  $V(\vec{r})$  is given by

$$(\Delta + k^2)\Psi(\vec{r}) = \frac{2\mu}{\hbar^2}V(\vec{r})\Psi(\vec{r}) \equiv U(\vec{r})\Psi \quad (3.1)$$

We assume that the potential  $U(\vec{r})$  falls rapidly to zero as  $r$  increases. At a large distance from the origin, the asymptotic solution to 3.1 can be written as:

$$\Psi(\vec{r}) = e^{ikz} + f(\theta, \varphi) \frac{e^{ikr}}{r} \quad (3.2)$$

This solution consists of the incoming wave (with the  $z$  axis as the incident direction) and also an outgoing scattered wave. The "scattering amplitude"  $f(\theta, \varphi)$  contains all the details about the scattering. The differential cross section  $\sigma$  is given by

$$\frac{d\sigma}{d\Omega} = |f(\theta, \varphi)|^2 \quad (3.3)$$

Now let us assume that  $V = V(r)$  is a central potential. Then we have axial symmetry and  $f$  is independent of  $\varphi$ . A general solution to equation 3.1 is then given by a superposition of products of radial functions and Legendre polynomials:

$$\Psi(r, \theta) = \sum_{l=0}^{\infty} (2l+1) i^l \frac{\chi_l(r)}{r} P_l(\cos \theta) \quad (3.4)$$

where  $\chi_l(r)$  satisfies the radial Schrödinger equation:

$$\chi_l'' + \left[ k^2 - U(r) - \frac{l(l+1)}{r^2} \right] \chi_l = 0 \quad (3.5)$$

For potentials that drop to zero faster than  $1/r$  as  $r \rightarrow \infty$ , one finds for the asymptotic form of  $\chi_l$

$$\lim_{r \rightarrow \infty} \chi_l = \frac{1}{k} A_l \sin(kr + \delta_l(k) - \frac{l\pi}{2}) \quad (3.6)$$

where  $A_l$  and  $\delta_l$  are real numbers. By inserting this ansatz into 3.2 one can derive the following expression for  $f(\theta)$ :

$$f(\theta) = \frac{1}{2ik} \sum_{l=0}^{\infty} (2l+1) (e^{2i\delta_l} - 1) P_l(\cos \theta) \quad (3.7)$$

This result is called the "partial wave expansion" of  $f(\theta)$  and implies that the scattering amplitude is completely characterized by the real phase shifts  $\delta_l$ . From  $f(\theta)$ , the total cross section can be calculated

$$\sigma_T = \frac{4\pi}{k^2} \sum_{l=0}^{\infty} (2l+1) \sin^2 \delta_l = \frac{4\pi}{k} \text{Im} f(0) \quad (3.8)$$

The second part of this equation is known as the "optical theorem".

In the s-wave limit where  $kr_0 < 1$  with  $r_0$  being the effective range of the potential, only the lowest partial wave contributes and  $\sigma_T$  reduces to

$$\sigma_0 = \frac{4\pi}{k^2} \sin^2 \delta_0 \quad (3.9)$$

If  $k$  goes to zero this yields

$$\lim_{k \rightarrow 0} \sigma_0 = 4\pi a^2 \quad (3.10)$$

where the "scattering length"  $a$  is given by

$$a = -\lim_{k \rightarrow 0} \frac{\tan \delta_0(k)}{k} \quad (3.11)$$

In the following two sections we want to introduce s-wave scattering resonances with



a simple model and discuss how such resonances effect the scattering cross section in the case of the contact interaction.

### Scattering Resonances: a simple model

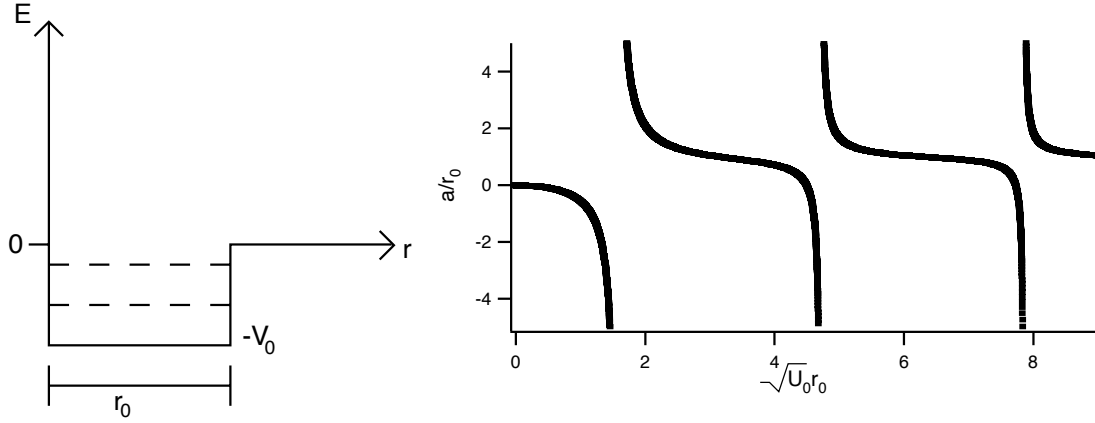


**Figure 3-1:** Whenever a new bound state with zero energy appears in the spherical potential well, the scattering length diverges.

Suppose the scattering potential is a spherical potential well

$$U(r) = \begin{cases} -\frac{2\mu V_0}{\hbar^2}, & r < r_0 \\ 0, & r > r_0 \end{cases} \quad (3.12)$$

In the s-wave limit, equation 3.5 gives the following radial equations:

$$\chi'' + (k^2 + U_0)\chi = 0 \quad (3.13)$$

$$\chi'' + k^2\chi = 0 \quad (3.14)$$

for  $r < r_0$  and  $r > r_0$  respectively. We require  $\chi(0) = 0$  and have

$$\chi_{r < r_0} = A \sin(\sqrt{k^2 + U_0} r) \quad (3.15)$$

$$\chi_{r > r_0} = B \sin(kr + \delta_0) \quad (3.16)$$

For  $r = r_0$  these solutions and their derivatives have to be continuous. This yields for  $\delta_0$ :

$$\tan \delta_0 = \frac{k(\tan(\kappa r_0) - \kappa r_0)}{k^2 r_0 \tan(\kappa r_0) + \kappa} \quad (3.17)$$

with  $\kappa = \sqrt{k^2 + U_0}$ . Thus  $a$  is given by

$$a = r_0 - \frac{\tan(\sqrt{U_0}r_0)}{\sqrt{U_0}} \quad (3.18)$$

Figure 3-1 shows the scattering length in units of  $r_0$ . For  $U_0 r_0^2 = \pi^2/4, 9\pi^2/4, \dots$  the scattering lengths diverges. But these are just the values of  $U_0 r_0^2$  where a new bound state with zero energy appears in the potential. For  $U_0 r_0^2 < \pi^2/4$  the potential is too shallow to support a bound state. One intuitively assumes that the potential in this case is attractive, which is indeed the case. If  $U_0 r_0^2$  is sufficiently large to just support a new bound state, the effective potential is repulsive.

Thus for attractive/repulsive interactions, the scattering length is negative/positive respectively and it diverges if a new bound state with zero energy appears.

### Contact interaction

The simplest approximation for the scattering of two particles with a large deBroglie wavelength  $\lambda_{dB}$  is the contact potential:  $V(\vec{r}) = c \cdot \delta(\vec{r})$ , where the constant  $c$  determines the strength of the interaction. Treating this potential mathematically is subtle and is described in [71]. For s-wave scattering, one obtains the following two equations:

$$\chi'' + k^2 \chi(r) = 0 \quad (3.19)$$

and the condition:

$$\chi''(0) = -\frac{c\mu}{2\pi\hbar^2} \chi'(0) \quad (3.20)$$

For the solution of equation 3.19, we make the ansatz

$$\chi = \frac{e^{(2i\delta_0)} e^{ikr} - e^{(-ikr)}}{2i} \quad (3.21)$$

which is up to an arbitrary phase factor proportional to  $\sin(kr + \delta_0)$ . Equation 3.20 requires

$$e^{2i\delta_0} = \frac{1 - ika}{1 + ika} \quad (3.22)$$

where  $a = \frac{c\mu}{2\pi\hbar^2}$ . Inserting this result in equation 3.7 yields

$$f = -\frac{a}{1 + ika} \quad (3.23)$$

and with equation 3.8

$$\sigma_0(k) = \frac{4\pi a^2}{1 + k^2 a^2} \quad (3.24)$$

Now let us calculate the scattering length:

$$-\lim_{k \rightarrow 0} \frac{\tan \delta_0}{k} = -\lim_{k \rightarrow 0} \frac{1}{ik} \frac{e^{2i\delta_0} - 1}{e^{2i\delta_0} + 1} = a \quad (3.25)$$

Thus the scattering length is identical to the constant  $a$  in the equations for the scattering amplitudes and the cross section. In fact  $\sigma_{\text{contact}}$ , evaluated for values of the scattering length  $a$  obtained from more complicated potentials, is in fairly good agreement with the actual cross sections [71].

If we increase the scattering length in equation 3.24, i.e. assume that  $ka \gg 1$  then the total cross section is limited by  $4\pi/k^2$ . So no matter how strong the interaction potential is or how large the scattering length becomes in the vicinity of a resonance, the upper limit on the cross section is  $\sigma_T = 4\pi(\lambda_{dB}/2\pi)^2$ . This is known as the "unitary limit".

### 3.1.2 BCS transition temperature and Feshbach resonances

#### BCS transition temperature

For a BCS transition, an attractive interaction between the atoms is required. This is the case if the scattering length  $a$  is negative. Then the critical temperature  $T_C$  for the BCS transition scales as [32]

$$T_C \simeq \frac{E_F}{k_B} \exp\left(-\frac{\pi}{2k_F|a|}\right) \quad (3.26)$$

$E_F, k_F$  are the Fermi energy and momentum respectively. This formula has been derived for dilute Fermi gases with  $n|a|^3 \ll 1$ . Since  $n \sim k_F^3$  this is equivalent to  $k_F|a| \ll 1$ . In an optical trap with a Fermi temperature of  $10\mu\text{K}$  and a typical scattering length of 100 Bohr radii  $a_0$ ,  $T_C/T_F$  is on the order of  $e^{-20}$ . Such temperatures are clearly experimentally unattainable. But equation 3.26 suggests that if  $a$  becomes large and negative, the exponential factor would be about unity and therefore  $T_C$  comparable to  $T_F$ . However, since in this regime  $k_F|a| \sim 1$ , equation 3.26 as originally derived is not applicable anymore. However, for large and negative  $|a|$ , transition temperatures up to  $0.5T_F$  have been predicted [33, 34, 35, 37, 38].

#### Feshbach resonances

The scattering length can strongly be modified in the vicinity of magnetic field dependent Feshbach resonances, which were originally studied for nuclear reactions [25]. In ultracold atomic gases, Feshbach resonances were first observed in  $^{23}\text{Na}$  [3].

For the two lowest ground state Zeeman levels,  $|1/2, -1/2\rangle$  and  $|1/2, 1/2\rangle$ , of  $^6\text{Li}$  an elastic s-wave Feshbach resonance has been predicted. The required magnetic field is below 1000 G [27, 26] and is experimentally achievable. In addition, the spin mixture of the two states is stable against spin exchange collisions. This makes  $^6\text{Li}$  a very promising candidate for the observation of a BCS transition [28, 29, 30].

At high magnetic fields the electronic and nuclear spins are decoupled and the atomic states in  $^6\text{Li}$  are numbered as shown in Figure 3-2. In this chapter we will refer to the  $|1/2, -1/2\rangle$  and  $|1/2, 1/2\rangle$  states as  $|2\rangle$  and  $|1\rangle$  respectively.

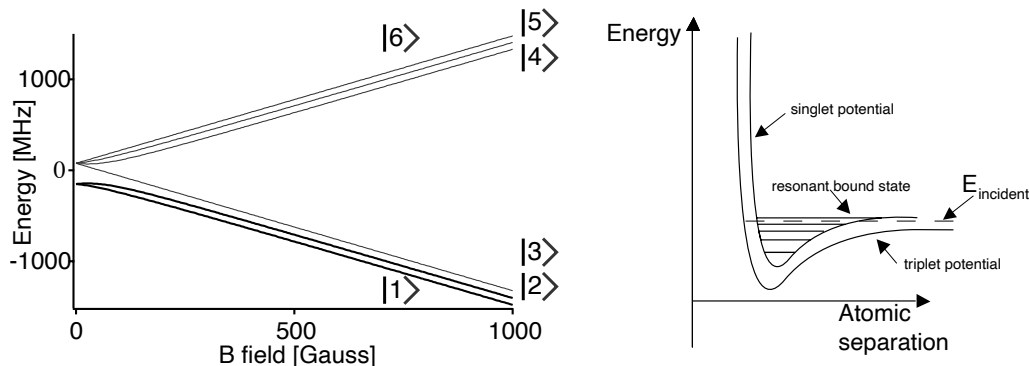


**Figure 3-2:** Left: Zeeman levels of the ground state of  $^6\text{Li}$ . The Feshbach resonance is predicted for states  $|1\rangle$  and  $|2\rangle$  which are high field seeking at magnetic fields above 27 G. Right: a schematic drawing of the two potentials involved in the scattering process. The singlet potential has a quasi-bound molecular state close to the dissociation limit that couples resonantly to the incident wave which is almost purely triplet.

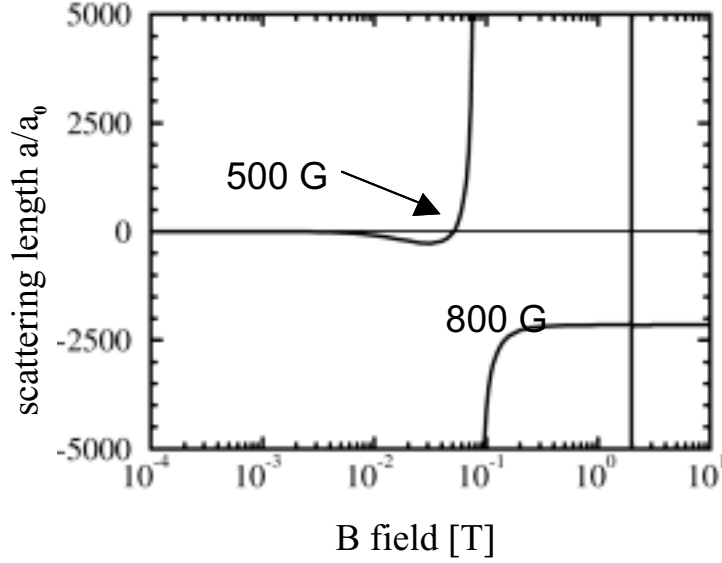
The interaction between two alkali atoms in their ground state is governed by the electronic singlet and triplet molecular potentials. In the case of the  $^6\text{Li}$  Feshbach resonance, the incoming wavefunction involving the antisymmetrized hyperfine states  $|1, 2\rangle$  is almost purely triplet. When its Zeeman energy is equal to the energy of a bound state of the singlet potential,  $|1, 2\rangle$  exhibits a Feshbach resonance and the scattering length diverges. The calculation for the location of the resonance was based on the experimentally determined singlet potential [26].

Figure 3-3 shows the predicted Feshbach resonance. The scattering length is given in units of the Bohr magneton and is plotted as a function of the magnetic field. For small fields, the scattering length is essentially zero, then it becomes negative with a minimum around  $-300a_0$ , crosses zero at about 500G and diverges around 800 Gauss. The scattering length above 800 G is large and negative, which implies strong and attractive interactions.

As can be seen from figure 3-2 the relevant states of  $^6\text{Li}$  are high field seeking at the magnetic fields of interest and therefore cannot be trapped in a magnetic trap. In order to perform the experiment, the atoms have to be transferred into an optical dipole trap (ODT) where they are trapped in the focus of a red detuned laser beam.

### 3.1.3 Signatures of Feshbach resonances

A standard technique to measure cross sections for elastic collisions is cross-dimensional thermalization [6, 41]. By changing the radial trap frequencies slowly compared to the atomic motion in the trap, energy is transferred or withdrawn from the atoms only in the radial dimension. During rethermalization the energy is redistributed between the axial and radial directions by elastic collisions. If the rate of these collisions is slow compared to the trap frequencies, this process can be



**Figure 3-3:** The predicted Feshbach resonance. Figure from [27].

monitored by observing the aspect ratio of the atomic cloud.

The rate of collisions is given by  $1/\tau = n\sigma v$ . In the ODT about  $10^5$  atoms are trapped at densities on the order of  $10^{13}/\text{cm}^3$  with trapping frequencies of several kHz. This yields a Fermi temperature of about  $10\mu\text{K}$  and leads to an estimate for  $v \sim \hbar k_F/m \sim 10\text{cm/s}$ . Assuming a scattering cross section of  $(2000a_0)^2$ ,  $1/\tau$  is on the order of several hundred kHz. Thus the condition for the observation of cross-dimensional thermalization is not fulfilled. Quite to the contrary, since  $\omega\tau < 1$  we are in the so called "hydrodynamic regime" and the method of cross-dimensional thermalization cannot be applied.

Furthermore at scattering lengths of  $2000a_0$ , which is roughly the background scattering length on the attractive side of the resonance, we approach the unitary limit. For  $T_F = 10\mu\text{K}$  the Fermi momentum is  $k_F \sim 2\pi/400\text{nm}$  and thus  $k_F a > 1$ . For larger scattering lengths, the cross section will quickly saturate at  $\sigma = 4\pi(\lambda_{dB}/2\pi)^2$ . For bosons, inelastic losses have been a striking signature of Feshbach resonances [3]. The lifetime of the atomic cloud close to the resonance was limited to a few microseconds [24]. A short lifetime of the  $^6\text{Li}$  cloud could impose severe limitations on the formation of Cooper pairs, which is expected to be on the order of a millisecond [31]. Therefore it was straightforward and important to look for an inelastic signature of the resonance.

## 3.2 Preparation of the spin mixture

The starting point for this experiment is about  $3 \cdot 10^5$   $^6\text{Li}$  atoms trapped in the  $|2\rangle$  state in the magnetic trap at a temperature of about  $400\text{nK}$  ( $1/2T_F$ ), while  $^{23}\text{Na}$  is

completely evaporated. The next step is to transfer the cloud into an optical dipole trap.

### 3.2.1 Transfer of Lithium into the ODT

#### Optical Dipole Traps

The physics of an optical dipole trap is based on the AC-Stark shift which can readily be understood within the dressed atom picture.

Let  $|g\rangle$  and  $|e\rangle$  be the ground and excited states of a two level atom described by the Hamiltonian  $H_A$ . Let  $|N\rangle$  denote the eigenstate of Hamiltonian  $H_L$  for laser mode L with N photons. We are now interested in the simultaneous eigenstates of the Hamiltonian  $H_A + H_L$  that describes the atom dressed with the laser field. These eigenstates are labeled as shown in figure 3-4.

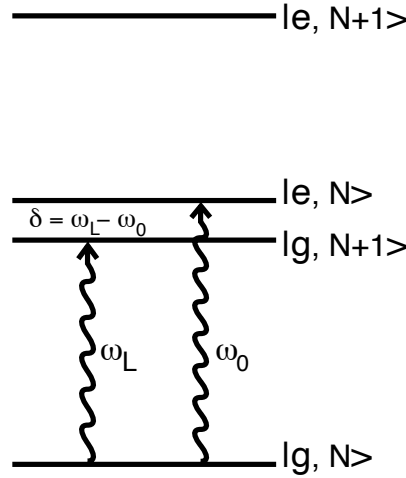


**Figure 3-4:** Energy levels in the dressed atom picture for an atom in a red detuned laser field close to resonance.  $\omega_0$  is the resonance frequency,  $\omega_L$  the laser frequency and  $\delta < 0$  the laser detuning which gives the separation between  $|g, N + 1\rangle$  and  $|e, N\rangle$ ;

The interaction Hamiltonian between the atom and the laser field is given by  $H_{int} = -\vec{d} \cdot \vec{E}$  with  $\vec{d}$  being the atomic dipole moment induced by the laser field. It resonantly couples the  $|g, N + 1\rangle$  and  $|e, N\rangle$  states, which in second order perturbation theory gives rise to an energy shift of the ground state proportional to:

$$\Delta E = \frac{|\langle e | \vec{d} | g \rangle|^2 E^2}{4\hbar\delta} \sim \frac{I}{\delta} \quad (3.27)$$

with  $I$  being the intensity of the laser. Since  $\Delta E < 0$  for  $\delta < 0$  atoms can be trapped in the intensity maximum, i.e. in the focus of a red detuned laser beam. For a blue detuned laser ( $\delta > 0$ ), the potential is repulsive. The quadratic dependence of the energy shift on  $E$  is analogous to the usual Stark effect. For a two level atom  $|\langle e | \vec{d} | g \rangle|^2$  is given by  $\frac{\hbar e^2}{2m\omega_0}$  and with  $I = \frac{c}{8\pi} E^2$  we get:

| power | $\varrho_0$      | $U_0$             | $\omega_r$ | $\omega_z$ |
|-------|------------------|-------------------|------------|------------|
| 1 W   | 14 $\mu\text{m}$ | 175 $\mu\text{K}$ | 12 kHz     | 200 Hz     |

**Table 3.1:** *ODT parameters*

$$U = -\frac{2\pi e^2}{mc} \frac{I}{2\omega_0(\omega_0 - \omega)} \quad (3.28)$$

For the ODT, a single beam of a diode pumped Nd:YAG laser at 1064nm wavelength is used. Its detuning from the atomic resonance (671nm for  ${}^6\text{Li}$ ) of  $8 \cdot 10^{14}\text{Hz}$  is huge compared to the fine structure splitting of the  $3^2\text{P}$  excited state (10GHz) and the hyperfine splitting of the  $2^2\text{S}_{1/2}$  ground state (228MHz). This justifies the two level approximation in the above derivation.

The intensity distribution in the focus of a Gaussian beam is given by:

$$I(\rho, z) = \frac{2P}{\pi \varrho_0^2 \left(1 + \left(\frac{z}{z_R}\right)^2\right)} \exp\left(-\frac{2\rho^2}{\varrho_0^2 \left(1 + \left(\frac{z}{z_R}\right)^2\right)}\right) \quad (3.29)$$

with P being the laser power,  $\varrho_0$  the  $1/e^2$  radius of the focus and  $z_R = \frac{\pi \varrho_0^2}{\lambda}$  the Rayleigh length. For  $z \ll z_R$  and  $\rho \ll \varrho_0$  this yields a cylindrically symmetric potential:

$$U(\rho, z) = -\frac{2e^2 P}{mc\omega_0(\omega_0 - \omega)\varrho_0^2} \left[1 - \left(\frac{z}{z_R}\right)^2 - 2\left(\frac{\rho}{\varrho_0}\right)^2\right] = \left[-U_0 + \frac{m}{2}\omega_\rho^2 \rho^2 + \frac{m}{2}\omega_z^2 z^2\right] \quad (3.30)$$

In this equation  $-U_0 = -\frac{2e^2 P}{mc\omega_0(\omega_0 - \omega)\varrho_0^2}$  gives the trap depths while  $\omega_z = \sqrt{\frac{2}{mz_R^2}U_0}$  and  $\omega_\rho = \sqrt{\frac{2}{m\varrho_0^2}U_0}$  are the axial and radial trapping frequencies respectively.

An extensive review on ODT's is given in [63]. Our ODT parameters are summarized in table 3.1.

### Transfer of the ${}^6\text{Li}$ atoms

We align the ODT horizontally along the symmetry axis of the magnetic trap. In order to facilitate the transfer of the atoms, we adiabatically decompress the latter in the radial direction. This results in an improved spatial overlap with the ODT beam. Its power is then adiabatically raised to its final value of 1W. Subsequently the magnetic fields are gradually turned off within 100ms. A finite axial guiding field of 1.5 G is provided by an external pair of coils. With this procedure, we can

transfer all the atoms from the magnetic trap into the ODT, yielding a peak density of  $3 \cdot 10^{13} \text{cm}^{-3}$ . The  $22 \mu\text{K}$  temperature of the cloud in the ODT, determined by fits to its axial line density profile, is slightly above the Fermi temperature of  $21 \mu\text{K}$ . This relative rise in temperature can be explained by excitations during the transfer. An absorption image of  $^6\text{Li}$  in the ODT is shown in figure 3-5.



**Figure 3-5:**  $^6\text{Li}$  atoms in state  $|2\rangle$  imaged in the ODT. The size of the cloud is about 1 mm axially and  $20 \mu\text{m}$  radially

### 3.2.2 Zeeman transfer and control of the spin mixture

For studying the inelastic decay, we were interested in three different spin compositions:

- a 50%-50% mixture of atoms in state  $|1\rangle$  and  $|2\rangle$ , for which the Feshbach resonance is predicted. A good control about the composition of this mixture is important not only for the purpose of this experiment: a possible BCS transition requires an equal number of atoms in both states.
- atoms either purely in state  $|2\rangle$  or in  $|1\rangle$ . These samples would reveal losses that are solely due to interactions within the same atomic state as well as technical losses.

Since initially only atoms in state  $|2\rangle$  are trapped in the ODT, they have to be transferred fully or in part to state  $|1\rangle$ . The latter was achieved with a non adiabatic rf-sweep across the center frequency of the ( $|1\rangle \leftrightarrow |2\rangle$ ) transition. In order to analyze the spin composition of the cloud, we reduced the strength of the optical confinement and separated the two states with an axial field gradient as shown in figure 3-6.

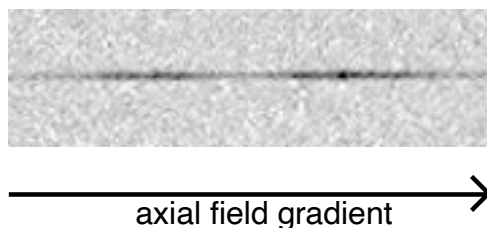


**Figure 3-6:** The  $|1\rangle$  and  $|2\rangle$  states of  $^6\text{Li}$  in the ODT separated by a magnetic field gradient.

We determined the atom numbers in the two states by resonant absorption imaging, taking the different transition strengths to the excited  $^2\text{P}_{3/2}$  state into account.



After adjusting the sweep parameters, we could control the spin composition of the mixture with an accuracy of  $\pm 4\%$ .

For the full transfer to state  $|1\rangle$ , an adiabatic Landau-Zener rf-sweep was applied, which was at least 95% complete.

### 3.3 Production of high magnetic fields

As can be seen from figure 3-3, magnetic fields up to 1000 G are required to exploit the full range of the Feshbach resonance. The only possibility to generate these fields on our machine was to use the coils of the magnetic trap. 1000 G could easily be reached by applying currents in the same direction through both antibias and curvature coils. However, the magnetic field produced by the curvature coils is axially anti-trapping for high field seeking states. Therefore we lost most of the atoms from the ODT after a magnetic field pulse. Using only the antibias coils, the curvature could be reduced by a factor of seven. This enabled us to trap the atoms in the ODT at all magnetic fields. In the next two sections, we will give more details about the setup of the magnetic fields and the field calibration.

#### 3.3.1 Feshbach circuit

A current of one Ampere through the antibias coils gives a magnetic field of 1.6G at the center of the trap. For magnetic fields up to 800 G we used one 30V, 500A Lambda EMI power supply, for higher fields, two of them were connected in parallel in a master-slave configuration. At the maximum output voltage of 30V, the 625 A required to achieve 1000 G were just within reach.

Figure 3-7 shows the electrical circuit diagram for curvature and antibias coils. To always have complete control over the spin composition of the atomic sample, we wanted to maintain the direction for the bias field throughout the experiment. However, in the normal trap configuration, the antibias coils produce a field in the opposite direction. Therefore, the current through the antibias coils for generating the high fields had to be reversed. This required the following changes to and extensions of the existing setup:

- Integrated Gate Bipolar Transistors (IGBT) Modules have been installed, capable of switching currents up to 1000 A in microseconds. The gate of each IGBT is powered on or off by a control circuit based upon a TTL-signal received from a control computer. If the magnetic fields are suddenly turned off, inductive voltage spikes can easily destroy an IGBT. Therefore a resistor and a diode are installed in parallel with the coils. If the IGBT opens, inductive currents are "rung down" by the resistance within 100  $\mu$ s.
- The reversed polarity of the Feshbach power supply required additional switches in the "ring down" paths for the curvature and the Feshbach power

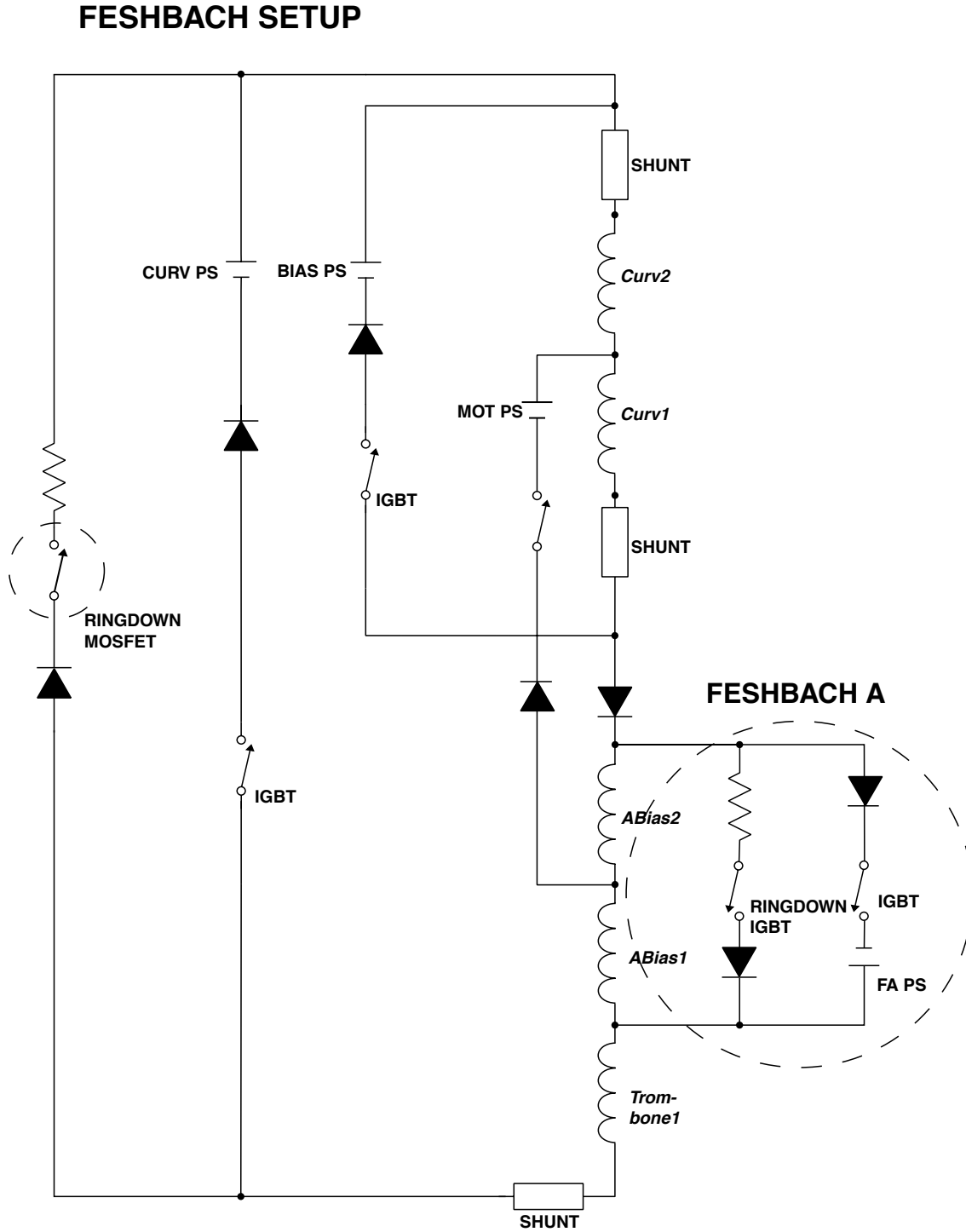


**Figure 3-7:** Shown is the the circuit for the antibias (*abias1*, *abias2*) and curvature (*curv1*, *curv2*) coils. During normal trap operation the curvature power supply (*CURV PS*) provides the current for both sets of coils connected in series. The connections of the coils ensure that the currents through antibias and curvature coils have the opposite sense. The bias power supply (*BIAS PS*) is used to apply an additional current through the curvature coils for catching the atoms from the MOT. The MOT field is generated with the current from the MOT power supply (*MOT PS*). Circled are the additions to the setup for the high magnetic field generation: the Feshbach power supply (*FA PS*), two IGBT's and one MOSFET solid state switch.

supply. Logic gates were built to prevent the Feshbach IGBT from opening if all other switches were not in the right state.

- All power supplies are operated in current mode and controlled by a 0-10V analog output from the control computer. The circuit setup requires that all power supplies are floating, i.e. that they are not referenced to ground. Therefore all of these analog control voltages have to be isolated from the computer control unit, which was done by differential amplifiers. During the first stages of setting up the experiment, a voltage spike related to high current switching destroyed the analog board of the computer. We therefore decided to replace the differential amplifiers by AD210 3-port isolation amplifiers (manufactured by Analog Devices). In this device, the channels for input, output, and power are galvanically separated, providing  $\pm 3500\text{V}$  (peak) common mode rejection. The signals and the power are transferred between the different units of the device via transformers.

To study inelastic losses at a certain magnetic field  $B_0$ , it is important to keep the interaction time for the atoms at fields below  $B_0$  at a minimum. This requires minimizing the time in which the power supplies change current. Therefore we programmed them to put out the desired current while the IGBT switch was still open. Their capacitors get precharged and the power supplies shoot up with the current when the switch is closed. To avoid overshoots, we limited the maximum voltage to a value that was just sufficient for supplying the desired current. The result is a rising time of about 6 ms for a current of 500 A (see figure 3-8).

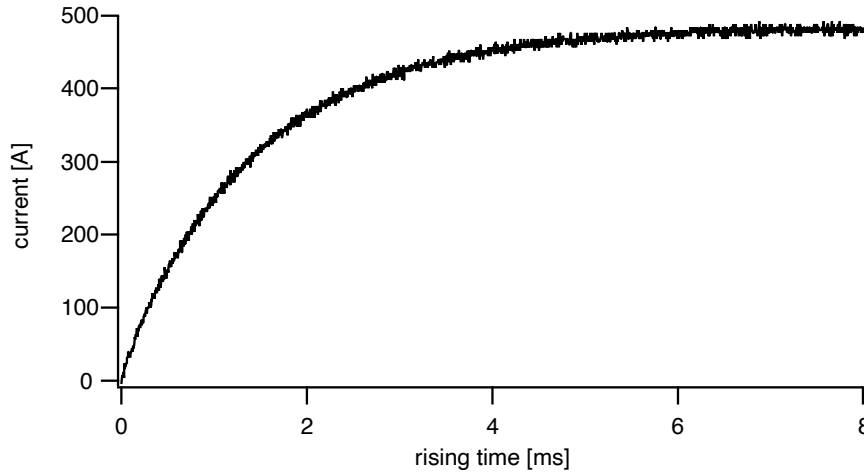


**Figure 3-8:** Current rise to about 500 A as a function of time, after the IGBT switch is opened.

This configuration enabled us to perform the experiments described below. However, the curvature of the antibias coils was still anti-trapping and required a stiff ODT, that had to be shifted away from its ideal zero field position to hold the atoms at

high fields. Also the water cooling of the coils was problematic. We could only keep the high currents on for a few seconds before overheating the coils.

### 3.3.2 High Field calibration

To calibrate the magnetic fields, two different techniques have been used. For fields below 100 G we applied rf-driven transitions in  $^{23}\text{Na}$  and for fields between 600 and 800 G we took absorption images of lithium in the ODT.

At a small bias field,  $^{23}\text{Na}$  was transferred in the  $|1, -1\rangle$  state from the magnetic trap into the ODT. Then we determined the center frequency of an rf-driven transition to the untrapped  $|1, 0\rangle$  state as a function of the applied magnetic field, while the current through the coils was monitored with a current clamp. The resonance frequency  $\omega_{res}$  was found by measuring the number of recaptured atoms in the magnetic trap. With the Breit-Rabi-formula,  $\omega_{res}$  was converted into a magnetic field:

$$\begin{aligned}\Delta E &= \hbar\omega_{exp} = E_{1,-1}(B) - E_{1,0}(B) \\ &= \hbar\omega_{hf} \left( \text{const} - \frac{1}{2}\sqrt{1-x+x^2} \right) - \left( \text{const} - \frac{1}{2}\sqrt{1+x^2} \right) \\ &= \frac{\hbar\omega_{hf}}{2} \left( \sqrt{1+x^2} - \sqrt{1-x+x^2} \right)\end{aligned}$$

where  $\omega_{hf} = 2\pi \cdot 1.77\text{GHz}$  is the hyperfine splitting and  $x = 2\mu_B B / (\hbar\omega_{hf})$ . The results are summarized in table 3.2

| Current<br>[A] | Resonance<br>frequency [MHz] | Magnetic<br>field [G] |
|----------------|------------------------------|-----------------------|
| 5              | 6.9                          | 9.8                   |
| 10             | 12.7                         | 18                    |
| 25             | 30                           | 42.2                  |
| 50             | 59.4                         | 82.7                  |

**Table 3.2:** Magnetic field calibration with a rf-driven transition in  $^{23}\text{Na}$ . The errors are  $\pm 11$  A on the current,  $\pm 0.5$  MHz on the resonance frequency and  $\pm 0.7$  G on the magnetic fields.

For the calibration of magnetic fields above 600 G we imaged  $^6\text{Li}$  with the slower and slower repumper light of the lithium laser system. These beams are red detuned from the  $2^2\text{S}_{1/2} (F=3/2) \rightarrow 2^3\text{P}_{3/2}$  transition by about 1 GHz and 772 MHz respectively. Their frequency difference is just the hyperfine splitting  $\omega_{hf} = 228$  MHz of the  $2^2\text{S}_{1/2}$   $^6\text{Li}$  groundstate. We imaged on the transitions  $(|1\rangle, |2\rangle) \rightarrow 2^3\text{P}_{3/2} m_j = -\frac{3}{2}$  (see figure 3-9).

Since the hyperfine splitting of the excited state at zero field is unresolved, we

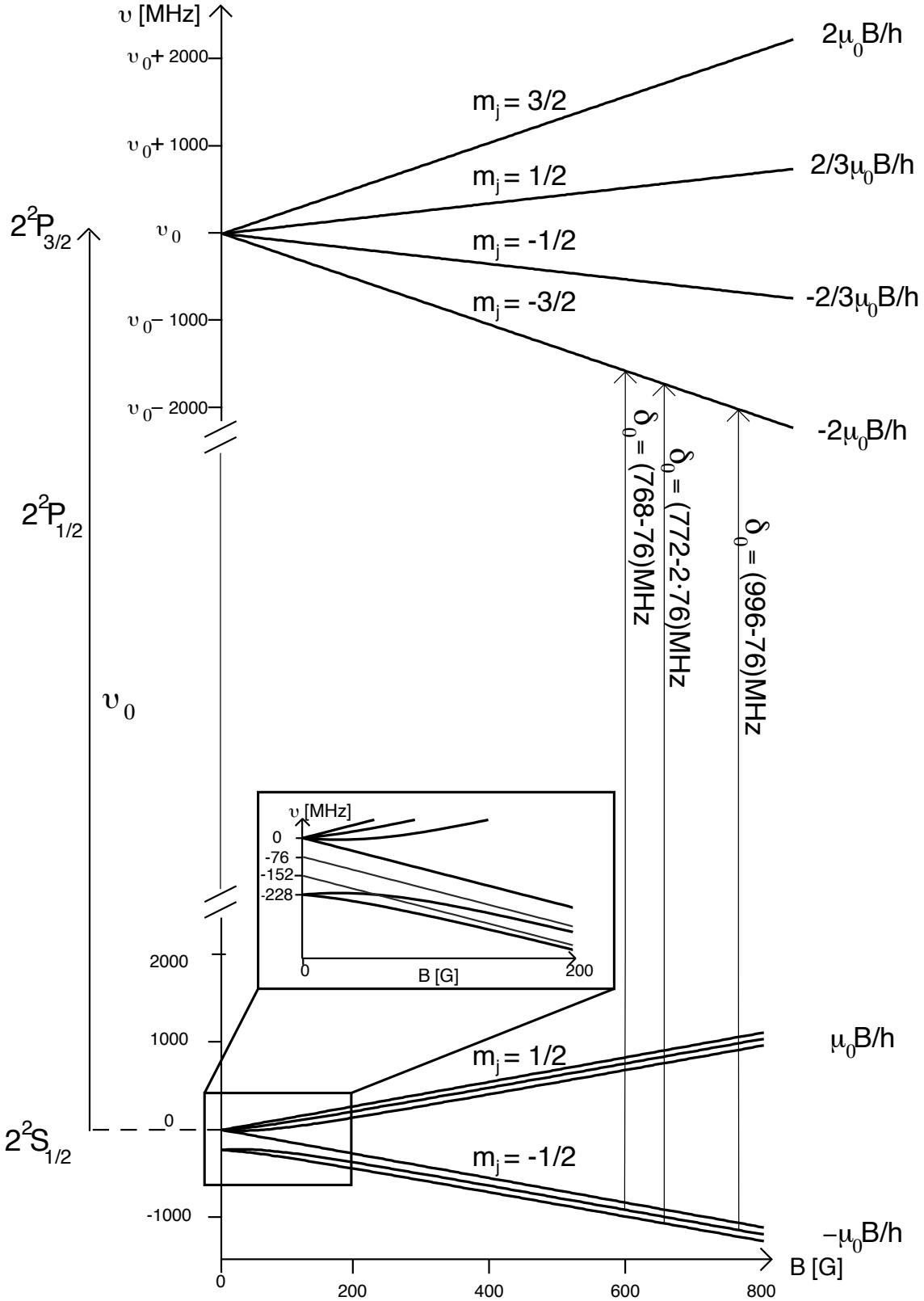


**Figure 3-9:** Magnetic field dependence of the ground and excited states of  $^6\text{Li}$ . The transitions used for the high field imaging are indicated. The inset shows the high field asymptotes to states  $|1\rangle$  and  $|2\rangle$ .

completely ignore the contribution of the nucleus to the excited level and label the states in the  $|j, m_j\rangle$  basis. For the ground state, however, one has to be more careful. The inset in figure 3-2 shows that at zero magnetic field, the asymptotes to states  $|1\rangle$  and  $|2\rangle$  have an appreciable offset from the  $^2S_{1/2}$ ,  $F = \frac{3}{2}$  level (for which  $\omega := 0$ ) of  $\Delta\omega_{|1\rangle} = -\frac{2\omega_{hf}}{3}$  and  $\Delta\omega_{|2\rangle} = -\frac{\omega_{hf}}{3}$  respectively. Taking this into account, we obtain the following approximations for fields above  $\sim 250\text{G}$ :

$$\begin{aligned}\frac{E_{|1\rangle}}{\hbar} &\approx -\frac{2\omega_{hf}}{3} - \frac{\mu_B B}{\hbar} \\ \frac{E_{|2\rangle}}{\hbar} &\approx -\frac{\omega_{hf}}{3} - \frac{\mu_B B}{\hbar} \\ \frac{E_{|3/2, -3/2\rangle}}{\hbar} &\approx \omega_0 - \frac{2\mu_B B}{\hbar}\end{aligned}$$

This yields transition frequencies of

$$\begin{aligned}\Delta\omega_{|1\rangle} &= \omega_0 - \underbrace{\left(\frac{\mu_B B}{\hbar} - \frac{2\omega_{hf}}{3}\right)}_{\delta_0} \\ \Delta\omega_{|2\rangle} &= \omega_0 - \underbrace{\left(\frac{\mu_B B}{\hbar} - \frac{\omega_{hf}}{3}\right)}_{\delta_0}\end{aligned}$$

where  $\delta_0$  is the detuning from the zero field resonance. To determine  $\delta_0$ , we applied a magnetic field close to the expected resonance and measured the absorption of the imaging light as a function of its detuning. With a Lorentian fit to the data we obtained  $\delta_0$ . The results are summarized in table 3.3 and figure 3-10.

| transition                                | current<br>[A] | $\delta_0$<br>[MHz] | magnetic<br>field [G] |
|---|----------------|---------------------|-----------------------|
| $ 1\rangle \rightarrow  3/2, -3/2\rangle$ | 365            | 768                 | 606                   |
|   | 465            | 996                 | 769                   |
| $ 2\rangle \rightarrow  3/2, -3/2\rangle$ | 400            | 772                 | 660                   |

**Table 3.3:** Magnetic field calibration with  $^6\text{Li}$  absorption imaging. The errors are  $\pm 1$  A on the currents,  $\pm 4$  MHz on the frequencies and  $\pm 3$  G on the magnetic fields.

Both calibration methods applied agreed within 2%, resulting in a magnetic field versus current ratio of 1.65 G/A. Magnetic field drifts occurring from thermal expansion of the coils due to resistive heating were found to be negligible.

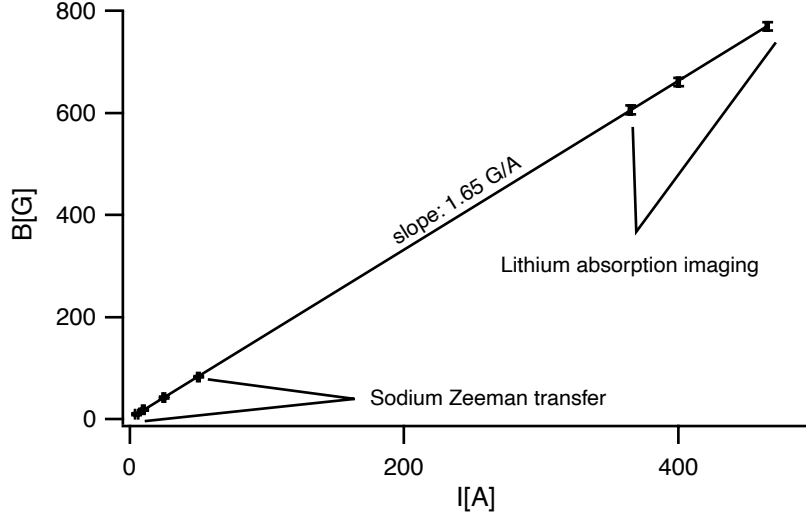


**Figure 3-10:** The magnetic field versus applied current. The slope is 1.65 G/A with 2% accuracy.

### 3.4 Magnetic field dependent decay of the $^6\text{Li}$ cloud

After the atoms were transferred into the ODT and the desired spin mixture was created, we subjected the atoms to magnetic fields between 200 and 900 G for different holding times. The fields were then switched off, leaving a small bias field to probe the remaining atoms by absorption imaging. Atom loss was monitored by measuring atom numbers for short (50 ms) and long (500 ms) magnetic field holding times. In order to be less sensitive to atom number drifts and initial losses from the optical trap, the number of atoms remaining after the long magnetic field pulse was normalized to the number after the short one.

Figure 3-11 shows the survival fraction for the different spin compositions as a function of the applied magnetic field. For a cloud purely in state  $|2\rangle$  (figure 3-11(a)), no significant loss was found over the entire range of magnetic fields. Strong magnetic field dependent losses were observed for the  $|1\rangle, |2\rangle$  spin mixture (3-11(c)). The most prominent feature is a broad, 100 G wide decay resonance at 680 G. A weaker and narrower, 20 G wide resonance at 550 G was revealed by a more detailed scan with an increased magnetic field holding time of 2 s (figure 3-11). At magnetic fields below 500 G no significant decay was observed. Above the strong resonance however, losses persisted at a constant level up to the highest applied magnetic field of 900 G.

The cloud of atoms in state  $|1\rangle$  showed a weak decay (21% loss at 680 G), identical to the position of the broad resonance in the mixture. This suggests a contamination of the cloud with atoms in state  $|2\rangle$ . However, a transfer efficiency from state  $|2\rangle$

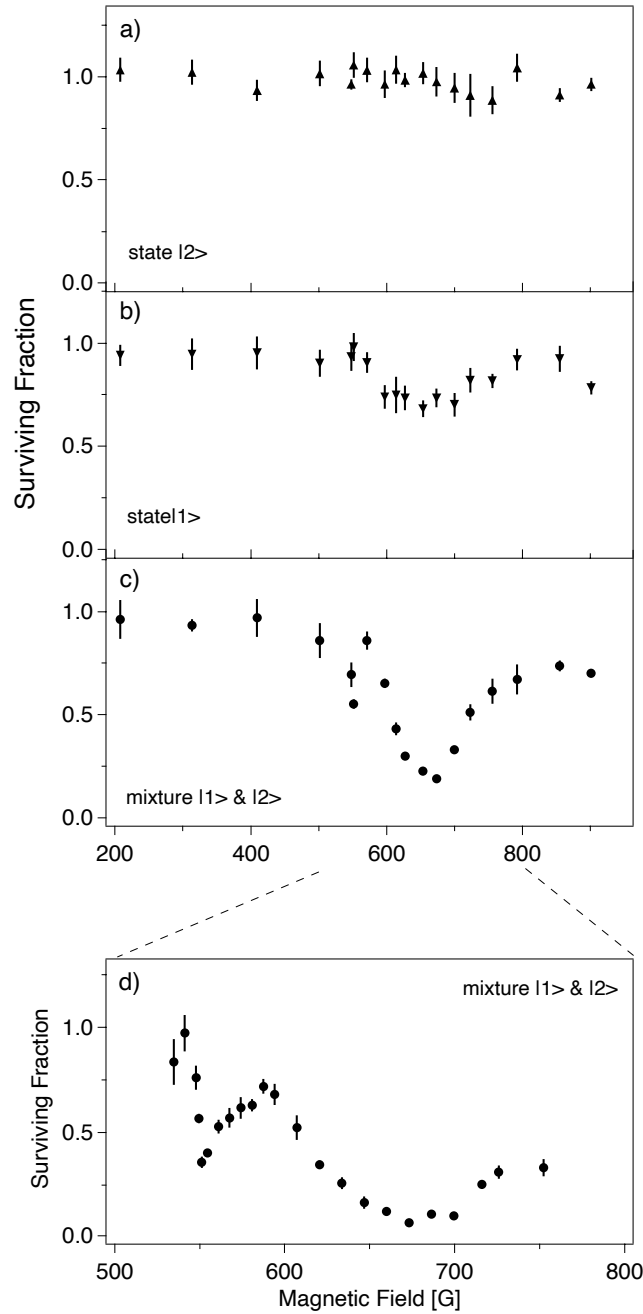


**Figure 3-11:** Magnetic field dependence of the inelastic decay. The fraction of atoms remaining after a 500 ms magnetic field pulse is shown for different spin compositions of the cloud a) For the state  $|2\rangle$ , no significant loss was observed. b) The energetically lowest state  $|1\rangle$  exhibits a weak decay resonance at  $\approx 680$  G. c) The 50% – 50% mixture of two spin states shows two decay resonances, at 550 G and 680 G. d) The two resonances are shown with higher density of data points and for 2 s magnetic field pulses. Each data point represents an average of three measurements.



to  $|1\rangle$  of more than 95% can only explain losses up to 15%, if three body decay is assumed.

### 3.4.1 Decay rates

To gain a better understanding of the nature of the losses in the spin mixture, we measured the decay rate of the atomic cloud at 680 G. For two-body decay, the loss rate of atoms  $\dot{N}$  is proportional to  $N^2$ , while for three-body decay, to  $N^3$ , where  $N$  is the number of trapped atoms. A linear time dependency of  $1/N$  or  $1/N^2$  therefore indicates a two- or three-body process respectively. As can be seen in figure 3-12, the data supports a two-body loss process.

In this context, it is also important to note that the spin mixture almost completely decays at the 680 G resonance. Starting from a 50%-50% mixture and assuming a simple three body decay this requires the two possible processes,  $(|1\rangle + |2\rangle) + |1\rangle$  and  $(|1\rangle + |2\rangle) + |2\rangle$ , to have almost equal amplitudes. Otherwise, the surviving fraction could not drop below 25%.

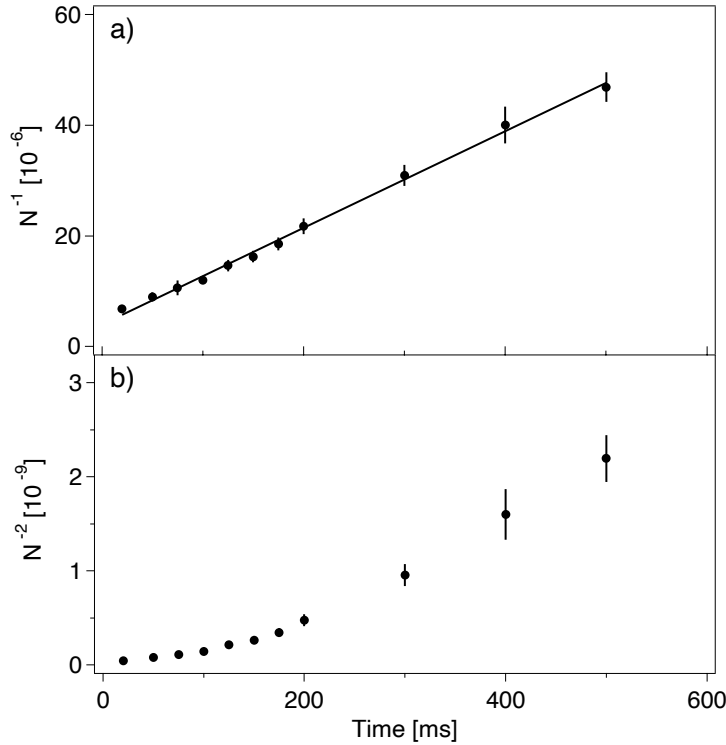


**Figure 3-12:** Decay of the atom number at 680 G. a) The data plotted as  $1/N$  show a linear time dependency, consistent with two-body decay. b) The same data plotted as  $1/N^2$  clearly show non-linear dependency, excluding simple three-body decay.

### 3.4.2 Discussion of the results and conclusion

At first sight, our results are not obviously related to the elastic Feshbach resonance predicted in [27]:

- we found two decay resonances instead of one
- the center of the broad resonance was observed at 680 G while the elastic resonance is predicted at about 800 G
- Our data support two-body decay; but the states  $|1\rangle$  and  $|2\rangle$  are the lowest energy states in  ${}^6\text{Li}$  and should not exhibit any inelastic two-body loss associated with an s-wave resonance

However, there is evidence that the observed losses are indeed a signature of the elastic Feshbach resonance. Improved theoretical calculations [19] take the recently measured zero crossing of the scattering length at about 530 G into account [17, 19] and exhibit a second, much narrower resonance at 550 G (see figure 3-13). This is in good agreement with the position of the narrow resonance we have observed.

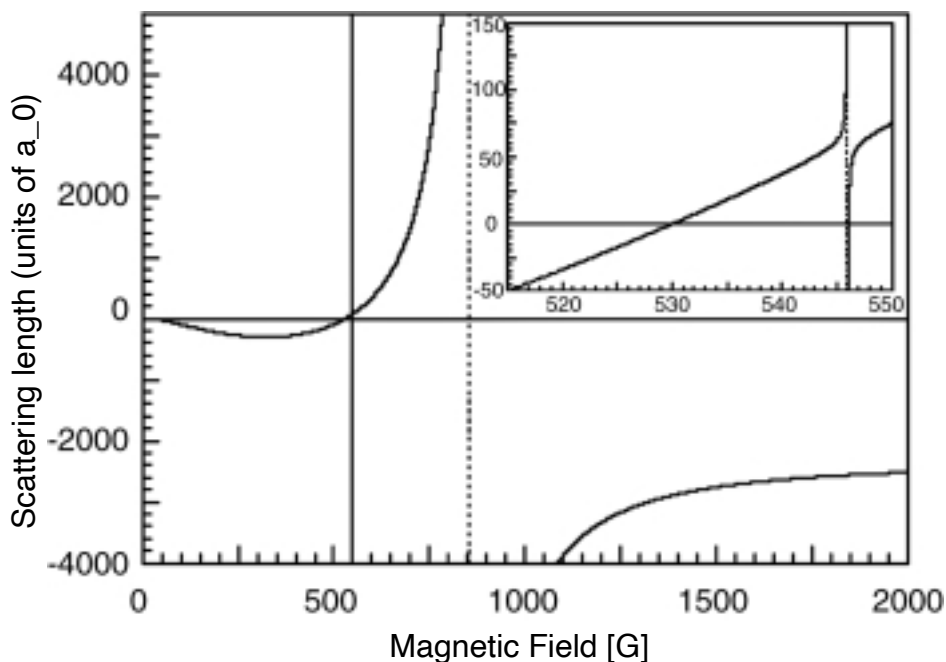


**Figure 3-13:** Result of an improved calculation of the scattering lengths for collisions in the  $|1\rangle$ ,  $|2\rangle$  mixture of  ${}^6\text{Li}$  as a function of the magnetic field. Figure adapted from [19].

The main resonance, now predicted for a magnetic field of 860 G, has a huge width. Therefore it seems plausible that the decay observed at 680 G (within this width) is related to this resonance.

Furthermore the only inelastic two-body process allowed in our system is dipolar relaxation in the p-wave channel:  $|2\rangle + |1\rangle \rightarrow |1\rangle + |1\rangle$  and  $|2\rangle + |2\rangle \rightarrow |2\rangle + |1\rangle$ . Since the kinetic energy of the cloud is on the order of the Fermi energy, p-wave collisions are not completely suppressed. However, no dipolar resonances are theoretically predicted [65]. Although our data do not support a simple three-body decay, it is possible that the losses are due to a two step three-body decay process as discussed in [39]. In such a process, the dependence of  $\dot{N}$  can be proportional to  $N^2$ , in agreement with our observations. In addition, it is not possible to attribute the decay resonances to evaporation, as they do not resemble the predicted magnetic field dependence for elastic collisions [19, 27].

The very good news from these measurements is that the time scale for the decay of the mixture - several hundred milliseconds - is long compared to the expected formation time of Cooper pairs in the one millisecond range. Therefore,  $^6\text{Li}$  is a promising candidate for further studies of elastic interactions in the vicinity of the Feshbach resonance [17, 19, 20] and the observation of a superfluid phase transition.



# Chapter 4

## The new magnetic trap

The magnetic trap used for the previously described Feshbach experiment had been installed on our machine in 1996 [42]. It had been designed for trapping and evaporative cooling of atoms, but not for studying phenomena at high magnetic fields. Nevertheless, it was possible to achieve the desired fields up to 1000 Gauss with the antibias coils of the trap. However, the trap was marginal for the experiments. Therefore I designed a new trap that was built after a coil of the old trap was shorted. This chapter contains a detailed description of the design and the features of the new trap.

### 4.1 The Design of the new trap

#### Design considerations

The new magnetic trap had to combine all desirable features of the old cloverleaf trap with modifications that allow for studying interacting fermions at fields up to 1000 Gauss. The old trap, was built to [43]

- provide the spherical quadrupole field for the MOT
- catch and trap the optically pre-cooled atoms
- allow for compression of the cloud to increase the collision rate for runaway evaporation at stable magnetic fields

The design had to satisfy the following conditions and restrictions:

- The optical access to the main chamber, for laser-cooling and imaging, had to be maintained
- The power dissipated in the coils had to be removed by efficient cooling.
- The currents that generate the magnetic fields had to be provided by commercially available power supplies.

- To allow for UHV conditions in the main chamber the trap had to be mounted outside of the vacuum chamber.

All these criteria have been met by the design of the old trap shown in figure 2-2 (the details can be found in [43]).

From our  ${}^6\text{Li}$  Feshbach experiment we learned, that a new trap should have these additional features:

- a higher magnetic field per unit current ratio for the antibias coils
- negligible gradient and curvature produced by the antibias coils
- improved water cooling

Further improvements included:

- higher radial gradients and axial curvature
- an easily adjustable “trombone” coil for the compensation of the offset fields of antibias and curvature coils
- an additional “trombone” coil for the compensation of an axial bias field due to imperfections of the cloverleaf coils

The goal was to increase the Gauss per Ampère ratio for the bias field produced by the antibias coils to at least 2.0 G/A. This would enable us to reach 1000G with the current of a single 30V-500A power supply (the ESS 30-500, manufactured by Lambda EMI, was already in use for the Feshbach experiment). At the same time the position of the coils had to be chosen to be as close as possible to an ideal Helmholtz configuration, to minimize axial gradient and curvature. Since the antibias coils are supposed to cancel the bias field of the curvature coils, the G/A coefficient for the curvature coils should ideally be a bit larger than 2.0 G/A.

## Calculations

In order to find the optimal positioning of the coils we calculated the magnetic fields for a variety of configurations. The possible designs were limited by the size of and by the distance between the two identical, recessed bucket ports into which each side of the trap had to fit. In addition, the finite size of the copper wire that we used for winding the coils had to be taken into account. The length of the coils was limited by their resistance and by the need for efficient water cooling. The details are summarized in appendix A.

## Results

It turned out that the only reasonable way to achieve the desired  $2G/A$  ratio for the antibias coils was, to move them as close to the atoms as possible, i.e. exchange their position with the one of the cloverleaf coils. However, since the rate of elastic collisions in the Ioffe-Pritchard trap scales as  $B'^{4/3}$ , where  $B'$  is the radial gradient generated by the cloverleaves, but only as  $B''^{1/3}$ , where  $B''$  is the axial curvature produced by the curvature coils, this is unfavorable for evaporative cooling. On the other hand, our main concern was not to optimize the design for the highest achievable collision rates. So, maintaining the same maximum gradient we obtained with the old trap seemed to be sufficient. By increasing the number of windings of the cloverleaf coils from twelve to sixteen each, and by using a 15kW instead of 10kW power supply to provide the current for the gradient coils, we could still expect an increase in the maximum available gradient.

The schematic design of the new trap is sketched in fig. 4-1. Antibias and curvature coils consist of ten windings each (2 axially and 5 radially), the cloverleaf coils of 16 windings each (4 axially and 4 radially).

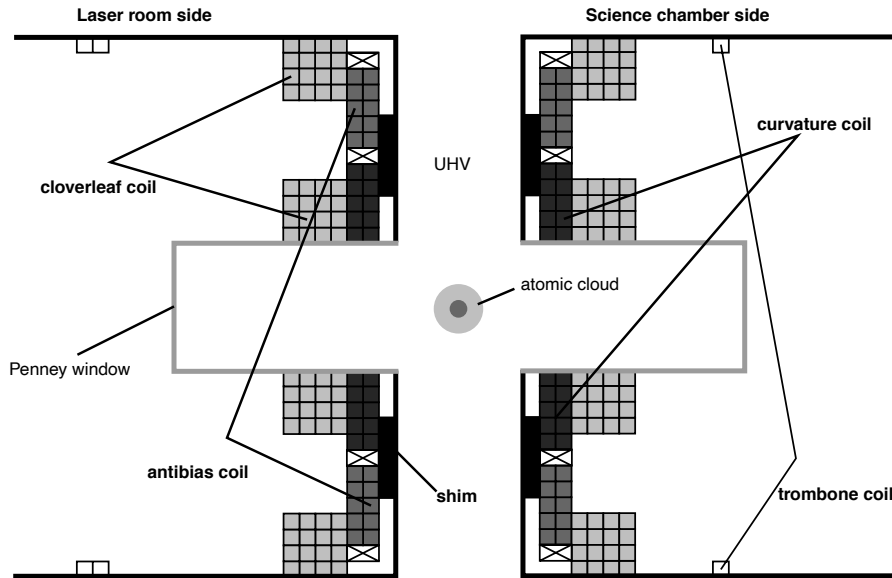


**Figure 4-1:** The schematic drawing shows a cut through the recessed bucket ports and the magnetic trap. The trap consists of two identical units. The two curvature coils (dark grey), the two antibias coils (in grey), four out of the eight cloverleaf coils (bright grey) and the two trombone coils (white) are indicated. Shims (black) were used to fine tune the distance between the two sides of the trap. The rectangles with a cross indicate the extra space that had to be allowed for, since the winding gives the coils a spiral shape.

By adjusting the radius of and the distance between the antibias coils, their magnetic field curvature could be significantly reduced. Figure 4-2 shows the calculated axial field of the old and the new antibias coils. It can be seen that the field of the old trap

was anti-trapping in the axial direction for high field seeking states. The new design gives improved values for all parameters of the trap. The results of all calculations are summarized in table 4.1.

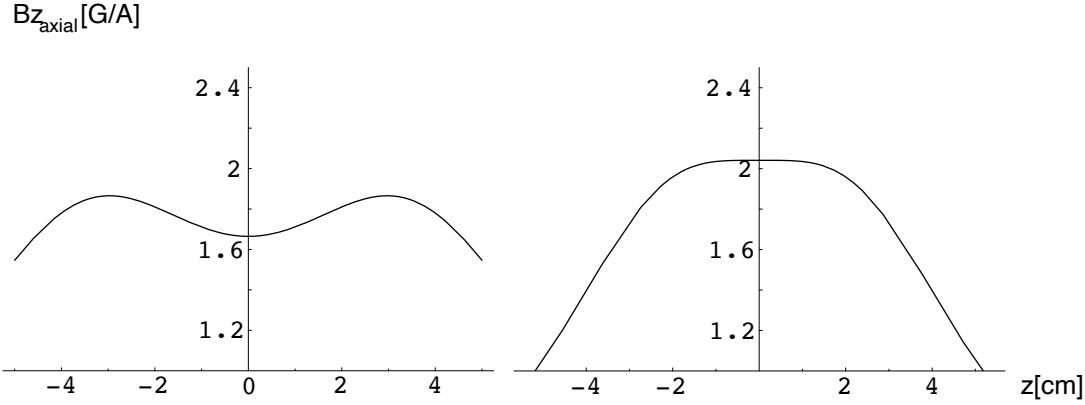


**Figure 4-2:** Axial field in G/A generated by the antibias coils of the old (left) and new (right) trap. The calculation was based on the expressions in appendix A.

| Coils        | Field           | New trap  | Old trap   |
|--------------|-----------------|---|--|
| curvature    | axial curvature | 0.82 G/cm <sup>2</sup> /A<br>(170 G/cm <sup>2</sup> ) | 0.48 G/cm <sup>2</sup> /A<br>(65 G/cm <sup>2</sup> ) |
|              | axial bias      | 2.06 G/A  | 1.6 G/A  |
| cloverleaves | radial gradient | 0.53 G/cm/A<br>(185 G/cm)                             | 0.56 G/cm/A<br>(135 G/cm)                            |
|              | axial curvature | 0.002 G/cm <sup>2</sup> /A                            | 0.07 G/cm <sup>2</sup> /A                            |
| antibias     | axial bias      | 2.04 G/A  | 1.6 G/A  |
|              | axial gradient  | 0.92 G/cm/A<br>(20 G/cm)                              | 0.6 G/cm/A<br>(20 G/cm)                              |
| MOT          |                 |   |  |
|              |                 |   |  |

**Table 4.1:** The magnetic fields to be produced by the new trap and the values of the old trap are given per Ampere and under typical operating conditions (in parenthesis).

## 4.2 Selection of materials and construction

All coils were wound by hand on a lathe around aluminum mandrels. We used hollow, square, insulated copper tubing with an outer side length of 1/8" and an inner side length of 1/16". Compared to circular tubing, square tubing allows for a more efficient packing of the coils. This results in a more homogenous current distribution and - because of the increased cross section - to a lower electrical resistance. The inner hole of the tube is used for water cooling of the coils. We decided to increase



the water flow through the antibiotics and curvature coils by splitting each of them into two independent subcoils (see section 4.2.2 for details). Thermocouples have been attached to the coils to monitor their temperature during the operation of the trap. In order to give each side of the trap a rigid structure, the coils were preassembled in a mold and then cast in epoxy, with the exception of the moveable trombone coils. For these a support structure was built that allowed for precise positioning. An additional plate was installed on the outside of the bucket ports to tightly secure the position of the trap. Finally, the copper tubes extending from the coils were silver soldered to circular copper tubing of 1/4" OD and 0.12" ID. The larger cross section of this tube gives a factor of 12 gain in conductivity and its circular shape allows for water connections with standard Swagelok components. The following paragraphs give more details about the manufacturing process. Figure 4-3 shows a photo of one side of the trap ready to be installed on the system.

### Winding the coils: technical details

**Cloverleaf coils:** The aluminum mandrel for the cloverleaf coils was cut out of an aluminum bar on a computer controlled milling machine (CNC) and then manually filed to its final size. In order to wind the copper wire flush around the mandrel, the wire was first bent around it and then hammered into its final position. Devcon "5 Minute Epoxy" was applied after each second layer of windings. This epoxy is rated to temperatures up to 90°C and cures within minutes, so that the winding process remains relatively fast.

**Antibias and curvature Coils:** For the curvature and antibiotics coils, the mandrels were machined out of aluminum rods that were turned down to the required diameters (29.6mm and 72.1mm respectively) on a lathe. Each coil was assembled out of two subcoils, which had five windings radially and one winding axially. The subcoils have independent electrical and water connections and have been wound in opposite senses. This allowed us to easily tie them together with kevlar thread. For achieving a strong and permanent bound by using epoxy resin, we could then take advantage of the large contact area between the two subcoils in the radial plane. Therefore, a strong epoxy of low viscosity was required. Our final choice was the Duralco NM 25 resin (produced by Cotronics). Its properties are summarized in table 4.2.

### Casting the trap

To ensure a stable configuration of the trap, first the relative position of the coils in each trap side had to be fixed, and second both sides of the trap had to be tightly secured in their respective bucket flanges. We cast both sides of the trap by pouring epoxy into a mold in which the coils of the trap were preassembled. The mold was built out of a hollow cast nylon tube with a slightly smaller inner radius than the bucket ports and a rod in its center, that had a slightly larger diameter than the penny window in the bucket flange. The position of the coils in the mold was

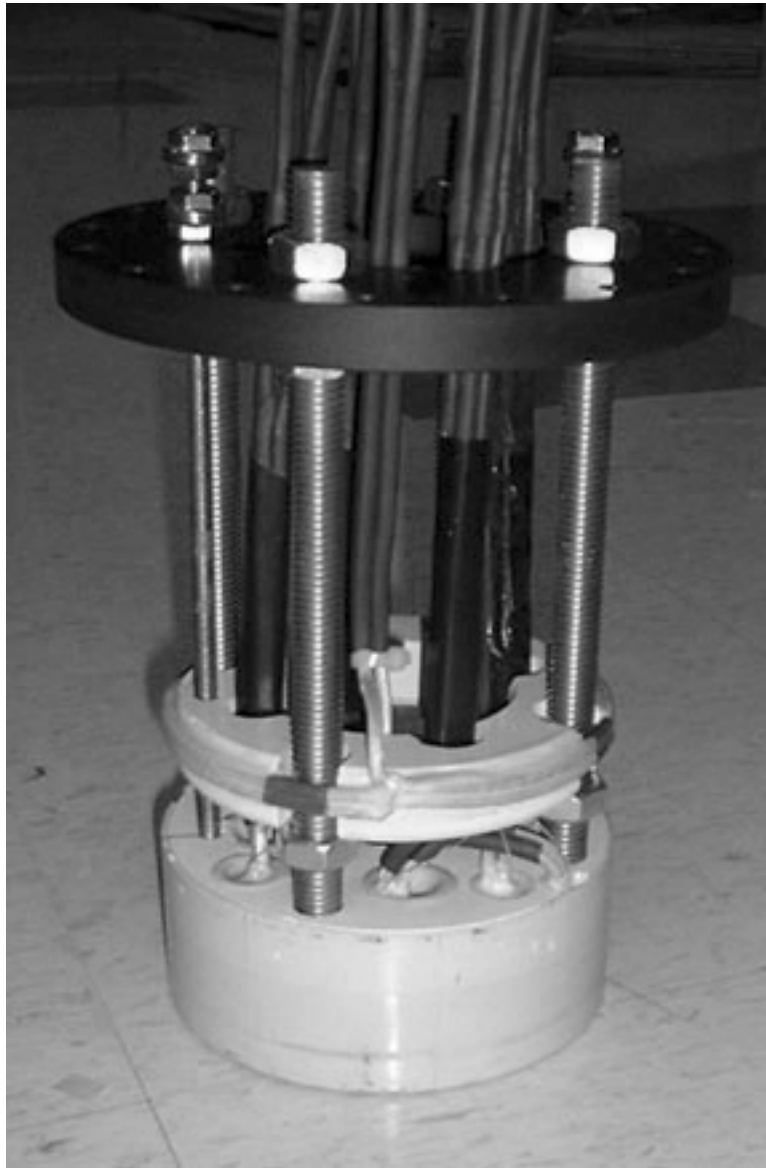


**Figure 4-3:** *Photo of one side of the new magnetic trap. The white cylindrical part contains the antibias, curvature, and gradient coils. The "trombone" coil can slide along the four brass rods extending from the backplate of the trap. The black plate mounted on top is used for securing the trap tightly into the vacuum flange.*

|                     |                                       |
|---------------------|---------------------------------------|
| temperature rating  | 260°C                                 |
| thermal expansion   | $6.4 \times 10^{-5}/^{\circ}\text{C}$ |
| dielectric strength | 500V/mil.                             |
| cure                | 4-16 hours at 22°C                    |

**Table 4.2:** *Some properties of the Duralco NM25 epoxy by Cotronics. This resin is free of magnetic particles or conductive fillers. With the help of a special thinner (105RT Resbond Thinner), its viscosity can be reduced.*

adjusted with the help of teflon spacers and adhesive kapton foil. A thermocouple was attached to each coil for future temperature monitoring.

For each side of the trap, a 3/4" thick backplate was machined out of glass-mica ceramics. This plate contained holes as a feed through for the copper wire and threaded holes for four 1/2"-13 brass rods, that were used to secure the position of the trap in the bucket flange. With the help of the epoxy the backplate was directly attached to the coils, so that they formed one single rigid unit.

Our first choice of the epoxy used for casting the trap was unfortunate: it was magnetic and easily magnetizable. We called its manufacturer, Cotronics, and learned that the problem was already known to them from the attempt to use it in HIFI loudspeaker manufacturing. Cotronics recommended the Duralco NM25 epoxy, already mentioned above (NM stands for non magnetic!, see table 4.2 for details). After rebuilding all the coils, the trap was cast in this epoxy.

The plates that were used to mount the trap sides onto the bucket flanges were machined out of 0.5" thick, glass filled polycarbonate plates. We attached them with nuts to the 1/2"-13 rods extending from the trap. Using sixteen 1/4"-20 tapped holes on the vacuum flange, we secured the trap in its final position.

### The "trombone" coils

The mandrel for the two "trombone" coils was machined out of a nylon tube (111.7mm outer diameter). After winding, each trombone coil was mounted on a 3/4" support ring of Glass-Mica ceramics, that was designed to slide along the 1/2"-13 rods extending from the back plate of the trap. Furthermore two 1/4"-20 holes were threaded into the support ring. Two 1/4"-20 brass rods, are screwed through this holes, with their ends rotating freely in two small holes in the back plate of the trap. By turning the 1/4"-20 rods, the trombone coils can be translated back and forth in a controlled manner.

### 4.2.1 Bench test of the new trap

#### Setup

The magnetic field measurements were performed with the 7030 Gauss/Tesla meter (manufactured by F.W.Bell) using the ZOA73-3208-05 three axis probe. Three mutually perpendicular (up to  $\pm 2^\circ$ ) Hall plates are placed in the probe's tip. For interpreting the data, one has to pay attention to the different positions of the Hall plates, since the offsets between the centers of the plates are up to 2.5mm. The active area of each probe is a disk of 1.5 mm radius and about 0.1 mm thickness. Both sides of the trap were mounted on translation stages to control their relative distance. The distance was set to 36.4mm, a value that was expected to minimize the curvature of the antibias coils. The probe position was controlled by a three-axes translation stage. The probe was moved in 1mm steps along the axial direction (in our experiment the y-axis) and two radial directions (with the x-axis corresponding to the slower axis and the z-axis to gravity).

#### The measurements

After aligning the probe, we first looked at the axial component of the magnetic field produced by the curvature coils. According to equation 2.5, this component should reach a minimum axially and a maximum radially. The minima/maxima of fits to the data gave the center of the curvature field. Ideally, the center of the cloverleaf coils, defined by the zero crossing of the radial gradient, should perfectly match. Since these gradients were measured with Hall plates different from the one used for the axial field, the offset in their position had to be subtracted from the data. On the x-axis, the radial difference in the centers was negligible, on the z-axis a remaining difference of about 0.3 mm was measured. Errors on this scale can easily be due to alignment issues of the two trap sides as well as of the hall probe relative to the trap.

#### Results

Figure 4-4 and table 4.3 give the results of the measurements. The curvature of the field generated by the antibias coils turned out to be as small as expected. Upper limits on inhomogeneities are a gradient of  $2 \cdot 10^{-3} \text{G}/(\text{cm A})$  and a curvature of  $5 \cdot 10^{-4} \text{G}/(\text{cm}^2 \text{A})$ . The radial gradient produced by the cloverleaf coils was measured along the x and z axes of the trap to be  $0.51 \text{G}/\text{cm}$ . A measurement of the axial bias field produced by the gradient coils seemed to support the assumption of a slight misalignment of the Hall probe with regard to the trap axis, rather than an actual offset field (upper limit  $2 \cdot 10^{-3} \text{G}/\text{A}$ ). The results are summarized in table 4.3 and are in very good agreement with the calculations. We concluded that two windings of the curvature trombone coil would be sufficient to adjust the axial offset field to 1 G. For the cloverleaf trombone coil, one axial winding was chosen.

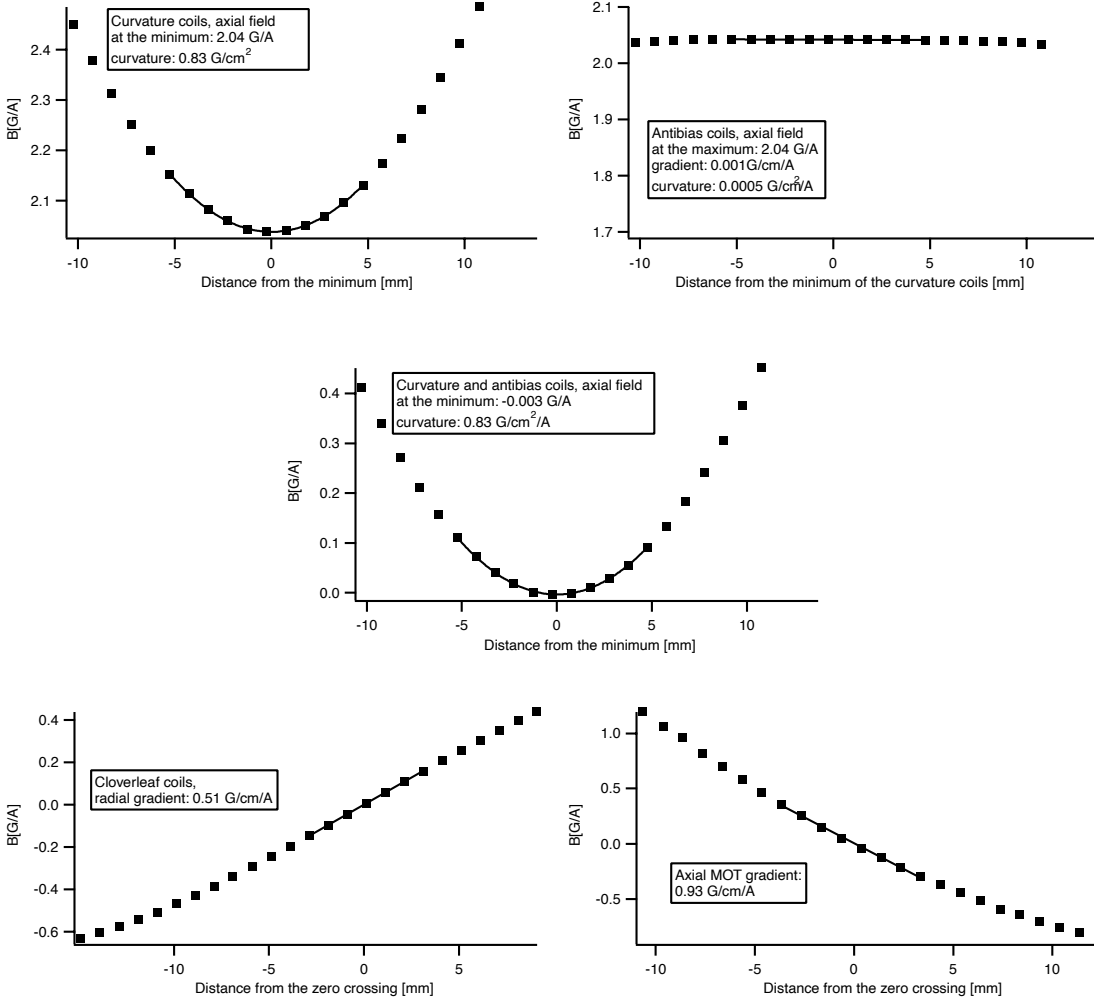


**Figure 4-4:** The results of the bench test of the trap. Shown are: the axial component of the magnetic field produced by the curvature coils along the axis of the trap, the same for the antibias coils and for curvature and antibias coils in series, the radial gradient of the cloverleaves along the radial direction and the axial MOT gradient (produced by one antibias and one curvature coil in anti Helmholtz configuration).

| Coils              | Field           | calculated                 | measured                    |
|--------------------|-----------------|----------------------------|-----------------------------|
| curvature          | axial curvature | 0.82 G/cm <sup>2</sup> /A  | 0.83 G/cm <sup>2</sup> /A   |
|                    | axial bias      | 2.06 G/A                   | 2.04 G/A                    |
| cloverleafs        | radial gradient | 0.53 G/cm/A                | 0.51 G/cm/A                 |
| antibias           | axial curvature | 0.002 G/cm <sup>2</sup> /A | 0.0005 G/cm <sup>2</sup> /A |
|                    | axial bias      | 2.04 G /A                  | 2.04 G/A                    |
| MOT                | axial gradient  | 0.92 G/cm/A                | 0.95 G/cm/A                 |
| gradient trombone  | axial bias      | 0.003-0.015 G/A            |                             |
| curvature trombone | axial bias      | 0.007-0.03 G/A             |                             |

**Table 4.3:** Comparison of calculated and measured trap parameters; tuning range of the trombone coils.

### 4.2.2 Water cooling

All coils of the trap are connected in parallel to the water cooling circuit. Since the flow through the coils is turbulent, the pressure depends quadratically on the flow:

$$p = \frac{1}{2}RQ^2 \quad (4.1)$$

with  $p$  being the pressure drop across the tube,  $R$  its resistance, and  $Q$  the flow.

Thus, splitting a given coil into two identical subcoils connected in parallel increases the flow in each coil by a factor of  $\sqrt{2}$ . With a total length of almost three meters each, the antibias coils were too long to be cooled efficiently in series. Therefore, we decided to split each of them into two subcoils. This turned out to be favorable for the winding of the coils itself and was also adopted for the curvature coils.

The water cooling should be sufficient to run the maximum current delivered by our 15 kW power supplies continuously through the coils. In a worst case scenario, one could assume that the total power is dissipated across four coils only (for example across the antibias coils during a Feshbach pulse). Therefore we decided that the water flow should be large enough to result in a temperature rise  $\Delta T$  of not more than 40 °C if about 4 kW of power are dissipated per subcoil. To get a very rough estimate of the required flow, we assumed  $W = Q \cdot c_V \cdot \Delta T$  and with the heat capacity of water  $c_V \simeq 4.2\text{kJ/l}$  one obtains a flow  $Q$  of about 1.5 l/min. To determine the required pressure, we measured the coil impedances and concluded that about 500 psi are sufficient.

To achieve these pressures at a total flow of about 40 l/min (for the whole trap), we bought a new booster pump manufactured by Webtrol (Model H15B40). At a flow of 10 gallons per minute this pump gives a pressure boost of 420 psi relative to its input pressure.

To distribute the high pressure water from the pump to the coils, we use about 15 m of 3/4" tubing rated to 2000psi. The large diameter of the tubing ensures that the pressure drop across it is negligible. On a water distribution panel, the water

is split up into 1/4" tubing that is connected to the coils. On the same panel, the water returning from the coils is joined into the low pressure return line. The flow of the returning water is measured for the purpose of a water flow interlock circuit (see below).

After the installation of the trap, this cooling system has been successfully implemented. Figure 4-5 shows the temperature rise of one of the antibias coils with increasing current. A diagram of the water circuit is given in appendix C.

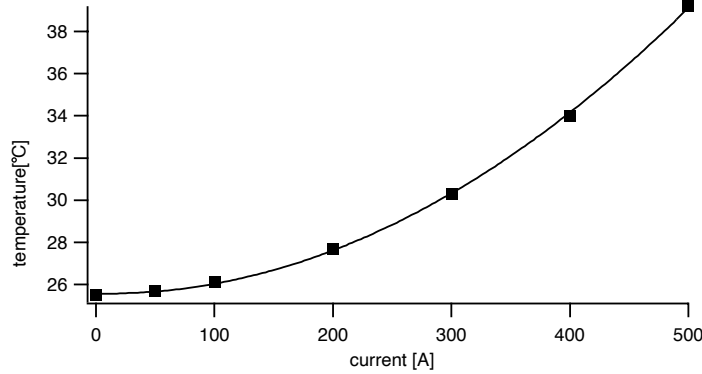


**Figure 4-5:** *Temperature of one of the antibias subcoils (antibias front, laser room side) as a function of the applied current. As expected, the temperature shows a quadratic dependence on the current. The total temperature rise is less than 14°C.*

### 4.3 Flow and temperature interlock

To assure a safe trap operation and to avoid any accidental overheating of the coils the flow of the cooling water through the coils is interlocked. If the flow drops due to clogging or a pressure drop in the system, the IGBT switches of all power supplies are opened. As can be seen in figure C-2, a total number of eleven flow meters are monitoring the flows through the coils, the Zeeman slower, and the cooling plates for the high power electronics and the cold plate in the oven region of the vacuum chamber. We use Model 101-7 flow meters manufactured by McMillan Company. Their original measuring range is 0.5-2 l/min. However, by adding a bypass in parallel, this range can be adjusted to higher values (1.25-5 l/min and 3-12 l/min). The flow meters deliver a voltage from 0-5 V proportional to the water flow. These voltages are read out by a Keithley 2700 Multimeter combined with a Model 7703 32-channel differential multiplexer module. This device allows for setting up a scan of the flow meter voltages by assigning each flow meter to a channel on the module. During a scan of the channels, the read voltage is compared to preset limits that can be specified independently for each channel. If an assigned limit is not met, the multiplexer outputs a TTL signal that is used to control the state of the IGBT switches. The scan speed is about 50 ms per channel.

In addition to the water interlock, we plan to set up a temperature interlock of the coils as well. During the manufacturing of the trap, a thermocouple has been attached to each coil. With the Keithley Model 7710 module, it will be possible to read out and interlock the coil temperatures using a setup similar to the one used for water flows.

## 4.4 Installation and operation of the new trap

In order to achieve the goal of a very small residual curvature of the antibias coils, the two sides of the trap had to be installed with the correct spacing. Therefore the distance between the two recessed bucket ports (see figure A-2) that hold the trap was measured. The spacing between the two sides of the trap was increased to the desired value with the help of shims as shown in figure 4-1. After installing the first side of the trap it became obvious, that we could not reach the desired sub-millimeter precision. Therefore, we decided to ensure, that the distance between the coils is rather too small than too large compared to the ideal value. This excluded the possibility of an anti-trapping curvature for the two lowest hyperfine states of  $^6\text{Li}$  at high magnetic fields. The change in the distance between the two trap sides, led to an increased imbalance between the bias field generated by the curvature and antibias coils. Therefore we had to use both, the curvature and the gradient “trombone” coils to support the antibias coils and adjust the bias field  $B_0$  to a value slightly above zero. This implied that we cannot separately compensate for a bias field produced by the gradient coils as originally intended. Fortunately, this bias field seems to be unnoticeable. Even a change in the direction of the currents through the cloverleaf coils, corresponding to a current difference of 700 A, didn’t change the total bias field. The observed increase in the bias field of the curvature versus the antibias coils leads to an estimate of the final distance between the two trap sides to be 35.8 mm. This goes along with slightly different values for the trap parameters: an axial bias field of 2.06 (2.10) G/A for the antibias (curvature) coils, an axial curvature of 0.84 G/(cm<sup>2</sup>A) and a gradient of 0.53G/(cmA).

The new trap allows us to subject the  $^6\text{Li}$  atoms to fields of 1030 G (at a current of 500 A), without observing any sloshing of the cloud or any other limitations. The maximum curvature of the field produced by the antibias coils is calculated to be 2.45G/cm<sup>2</sup> at a magnetic field of 1030 G. Furthermore a recent calibration of the magnetic fields confirmed the 2.06 G/A ratio for the antibias coils.

In conclusion, the new magnetic trap met all of its design criteria and provides the homogeneous magnetic fields required for the study of strongly interacting fermions.



# Chapter 5

## Conclusion and Outlook

In this thesis we have described experiments with fermionic  ${}^6\text{Li}$  atoms, that are sympathetically cooled in a magnetic trap by a reservoir of bosonic  ${}^{23}\text{Na}$  atoms. Simultaneous quantum degeneracy of a large and stable  ${}^{23}\text{Na}$  BEC and a  ${}^6\text{Li}$  Fermi sea is achieved. We have optically trapped the two lowest hyperfine states of  ${}^6\text{Li}$  and have subjected this spin mixture too magnetic fields up to 900 G. The observed magnetic field dependent losses at 550 and 680 G are interpreted as a signature of two theoretically predicted, elastic s-wave Feshbach resonances. The lifetime of the spin mixture at magnetic fields at which a large and negative scattering length is predicted exceeds 100 milliseconds. Since the time expected for Cooper pair formation is at least two orders of magnitudes smaller,  ${}^6\text{Li}$  is a promising candidate for the observation of a BCS-like superfluid phase transition.

After the installation of the new magnetic trap, we are now able to resume the study of  ${}^6\text{Li}$  at high magnetic fields. After the transfer to the optical trap, we keep the  ${}^6\text{Li}$  atoms in the  $|2\rangle$  state while the magnetic fields are switched on. This strategy excludes any limitations due to the observed decay resonances in the spin mixture. The mixture is created at magnetic fields above 900 G and we observe cooling due to evaporation. Furthermore, we can now image both states of the mixture simultaneously at high magnetic fields. This should allow us to study elastic interactions as recently reported in [20].

The possibilities for further experiments are rich: The interaction properties of the  ${}^{23}\text{Na}$  BEC with  ${}^6\text{Li}$  Fermi sea can be explored. Strong interactions between quantum degenerate  ${}^{40}\text{K}$  and  ${}^{87}\text{Rb}$  clouds have been reported [23]. Furthermore optical lattices offer a different method to tune the interactions in ultracold Fermi clouds as proposed in [40].



# Appendix A

## Calculation of the magnetic fields

### A.1 Circular coils

The magnetic field on the symmetry axis of a circular coil of radius  $r$ , generated by a current  $I$  can be calculated with Ampère's law to be

$$B_z(0, 0, z) = \frac{\mu_0 I}{2r} \left(1 + \left(\frac{z - z_0}{r}\right)^2\right)^{-3/2} \quad (\text{A.1})$$

where  $z_0$  is the position of the coil. In order to obtain an expression for a finite sized coil of thickness  $t$  and length  $l$ , this equation can be integrated, axially in the boundaries from  $z_0 = z_c - l/2$  to  $z_0 = z_c + l/2$  and radially from  $r = r_{min}$  to  $r = r_{max}$ . In these expressions  $d$  gives the position of the center of the coil and  $r_{min}$  ( $r_{max}$ ) are the inner (outer) radii of the coil. A homogeneous current density of  $j = NI/Lt$  is being assumed ( $N$  being the number of windings of the coil and  $t = r_{max} - r_{min}$ ). This yields [45]:

$$B_z(0, 0, z) = \frac{\mu_0 I N r_{min}}{2Lt} \left\{ x_2 \ln \left[ \frac{x_2}{x_1} \frac{1 + \sqrt{1 + x_1^2}}{1 + \sqrt{1 + x_2^2}} \right] - x_4 \ln \left[ \frac{x_4}{x_3} \frac{1 + \sqrt{1 + x_3^2}}{1 + \sqrt{1 + x_4^2}} \right] \right\} \quad (\text{A.2})$$

with  $x_1 = (z - z_c + L/2)/r_{max}$ ,  $x_2 = (z - z_c + L/2)/r_{min}$ ,  $x_3 = (z - z_c - L/2)/r_{max}$ ,  $x_4 = (z - z_c - L/2)/r_{min}$ . This equation and its derivatives have been used to calculate the magnetic fields, field gradients and curvatures, of antibiotics, curvature and trombone coils.

### A.2 Cloverleaf coils

The magnetic field produced by the cloverleaf coils, has been calculated with the law of Biot and Savart:

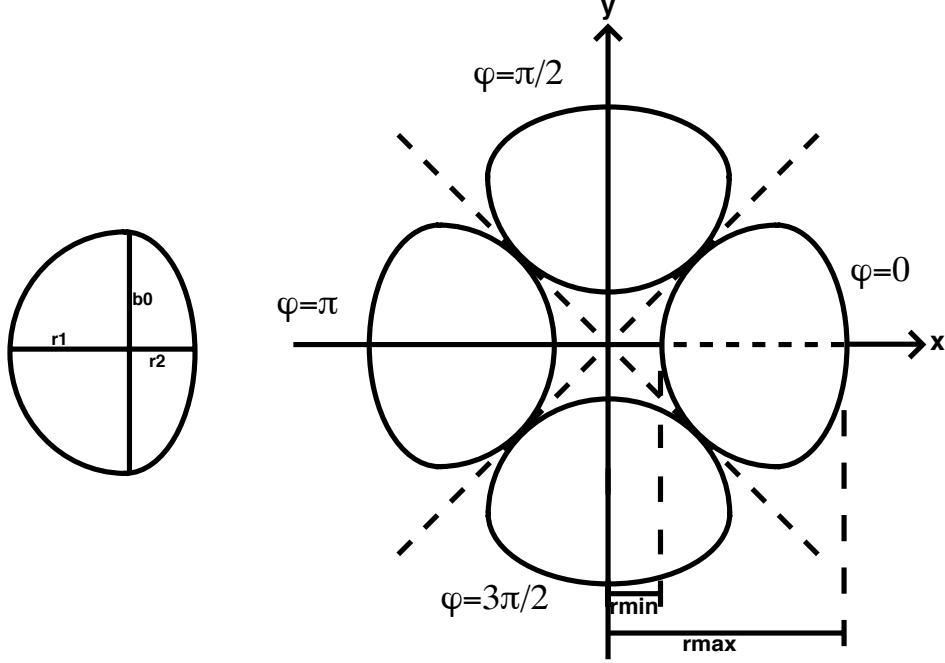


**Figure A-1:** Definition of  $b_0, r_1, r_2$  for a single cloverleaf coil (left) and positions of a set of four cloverleaf coil (right).

$$\vec{B} = \frac{\mu_0 I}{4\pi} \int \frac{d\vec{r}' \times (\vec{r} - \vec{r}')}{|\vec{r} - \vec{r}'|^3} \quad (\text{A.3})$$

In order to calculate the fields for thick wires a brute force approach was chosen: For each winding of the cloverleaf coil the square cross section of the wire was divided into a grid of 25 cells. The center of each cell gives the position of one infinitely thin loop carrying a current of  $I/25$ . The contributions of each of these loops to the magnetic field were summed up.

I have chosen the following parameterization of the cloverleaf coils: their shape can be described as composed of two half ellipses with the same major axis ( $b_0$ ) but different minor axes ( $r_1$  and  $r_2$ ) as shown in figure A-1. The sum of the minor axes is given by the difference of  $r_{max}$  and  $r_{min}$ , where  $r_{min}$  and  $r_{max}$  are the smallest and largest radial distances between a coil and the  $z$  axis.  $r_{min}$ ,  $r_{max}$ , and  $r_1$  are treated as free parameters. The radius of the major axis  $b_0$  is determined according to the condition that the four cloverleaf coils don't touch each other. This yields:  $b_0 = \sqrt{2r_1 r_{min} + r_{min}^2}$ . The position of the coils is given by the position of the intersection of their major and minor axis. In cylindrical coordinates:  $(r = r_{min} + r_1, \varphi = 0, \pi/2, \pi, 3\pi/2, z = \pm d_0/2)$ .  $d_0$  is the smallest distance between the two sets of cloverleaf coils on each side of the trap.

The arclength vector of an ellipse with axes  $a_t^i$  and  $b_t^i$  is given by:

$$\vec{e}_t^i = \begin{pmatrix} -a_t^i \sin \varphi \\ b_t^i \cos \varphi \\ 0 \end{pmatrix} \quad (\text{A.4})$$

The vector from the current source point

$$\begin{pmatrix} a_t^i \cos \varphi + \Delta x \\ b_t^i \sin \varphi + \Delta y \\ z_d \end{pmatrix} \quad (\text{A.5})$$

to the magnetic field point  $\vec{x} = (x, y, z)$  is given by:

$$\vec{r}_{t,d}^i = \begin{pmatrix} x - a_t^i \cos \varphi + \Delta x \\ y - b_t^i \sin \varphi + \Delta y \\ z - z_d \end{pmatrix} \quad (\text{A.6})$$

The magnetic field produced by the coils with  $m_r$  radial and  $n_z$  axial windings at a current  $I = 25I'$  given by:

- for  $\varphi = 0$  and  $\varphi = \pi$ :

$$\vec{B}_{\varphi=0,\pi,z=\pm d_0/2}(x, y, z) = \frac{\mu_0 I'}{4\pi} \sum_{t=0}^{(5m_r-1)} \sum_{d=0}^{(5n_z-1)} \left( \int_{-\pi/2}^{\pi/2} \frac{\vec{e}_t^2 \times \vec{r}_{t,d}^2}{|\vec{r}_{t,d}^2|^3} d\varphi + \int_{\pi/2}^{3\pi/2} \frac{\vec{e}_t^1 \times \vec{r}_{t,d}^1}{|\vec{r}_{t,d}^1|^3} d\varphi \right) \quad (\text{A.7})$$

- for  $\varphi = \pi/2$  and  $\varphi = 3\pi/2$ :

$$\vec{B}_{\varphi=\pi/2,3\pi/2,z=\pm d_0/2}(x, y, z) = \frac{\mu_0 I'}{4\pi} \sum_{t=0}^{(5m_r-1)} \sum_{d=0}^{(5n_z-1)} \left( \int_0^\pi \frac{\vec{e}_t^2 \times \vec{r}_{t,d}^2}{|\vec{r}_{t,d}^2|^3} d\varphi + \int_\pi^{2\pi} \frac{\vec{e}_t^1 \times \vec{r}_{t,d}^1}{|\vec{r}_{t,d}^1|^3} d\varphi \right) \quad (\text{A.8})$$

Table A.1 gives the values for  $a_t^1, a_t^2, b_t^1, b_t^2, \Delta x, \Delta y$  that have to be substituted into A.7 and A.8 for the different values of  $\varphi$ . To calculate the magnetic field produced by all eight cloverleaf one has to take the desired sense of the currents into account:

$$\vec{B}(x, y, z) = \vec{B}_{\varphi=0,z=\frac{d_0}{2}} - \vec{B}_{\varphi=0,z=-\frac{d_0}{2}} + \vec{B}_{\varphi=\pi,z=\frac{d_0}{2}} - \vec{B}_{\varphi=\pi,z=-\frac{d_0}{2}} \quad (\text{A.9})$$

$$- \vec{B}_{\varphi=\pi/2,z=\frac{d_0}{2}} + \vec{B}_{\varphi=\pi/2,z=-\frac{d_0}{2}} + \vec{B}_{\varphi=3\pi/2,z=\frac{d_0}{2}} - \vec{B}_{\varphi=3\pi/2,z=-\frac{d_0}{2}} \quad (\text{A.10})$$

| position           | $a_t^1$          | $a_t^2$          | $b_t^1$          | $b_t^2$          | $\Delta x$         | $\Delta y$         |
|--------------------|------------------|------------------|------------------|------------------|--------------------|--------------------|
| $\varphi = 0$      | $r_1 - \delta t$ | $r_2 - \delta t$ | $b_0 - \delta t$ | $b_0 - \delta t$ | $(r_{min} + r_1)$  | 0                  |
| $\varphi = \pi$    | $r_2 - \delta t$ | $r_1 - \delta t$ | $b_0 - \delta t$ | $b_0 - \delta t$ | $-(r_{min} + r_1)$ | 0                  |
| $\varphi = \pi/2$  | $b_0 - \delta t$ | $b_0 - \delta t$ | $r_1 - \delta t$ | $r_2 - \delta t$ | 0                  | $(r_{min} + r_1)$  |
| $\varphi = 3\pi/2$ | $b_0 - \delta t$ | $b_0 - \delta t$ | $r_2 - \delta t$ | $r_1 - \delta t$ | 0                  | $-(r_{min} + r_1)$ |

**Table A.1:** The radial position of the coils is given by:  $r = (r_{min} + r_1)$ . If  $z = \pm d_0/2$ , then  $z_d = \pm(d_0/2 + \delta d)$ .  $\delta = s/5$  with  $s$  the side length of the square wire used for winding the coils. To the values given in the columns for  $a_t^1$ ,  $a_t^2$ ,  $b_t^1$ ,  $b_t^2$  the constant  $\delta/2$  has to be added.

To finally obtain the radial gradient  $B_x(x_0, 0, 0)/x_0$  was evaluated with  $x_0 = 0.001\text{cm}$ .

### A.3 Parameters for the calculation and results

The trap had to be designed to fit into the recessed bucket ports. The relevant parameters are summarized in Figure A-2. The square copper wire used for winding the coils has a side length of 0.35cm (including its insulation). A to scale drawing of the coil distribution in one trap side is given in Figure A-3.

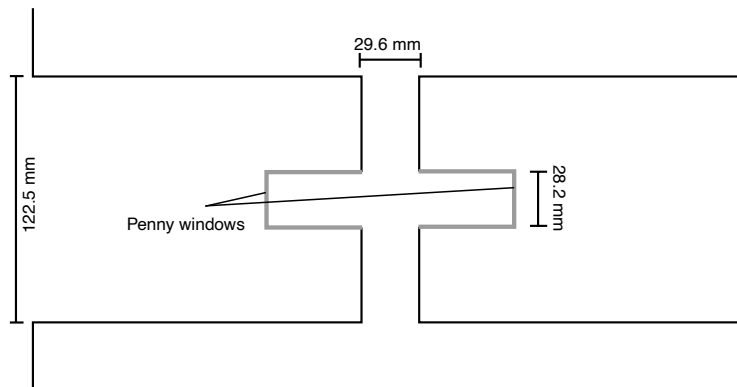


**Figure A-2:** The two vacuum (bucket) flanges into which the magnetic trap had to fit. The distance between the flanges (including the wall thickness) is 29.6 mm. The grey part in the drawing indicates the penny windows that are used for the horizontal MOT beams and side imaging.

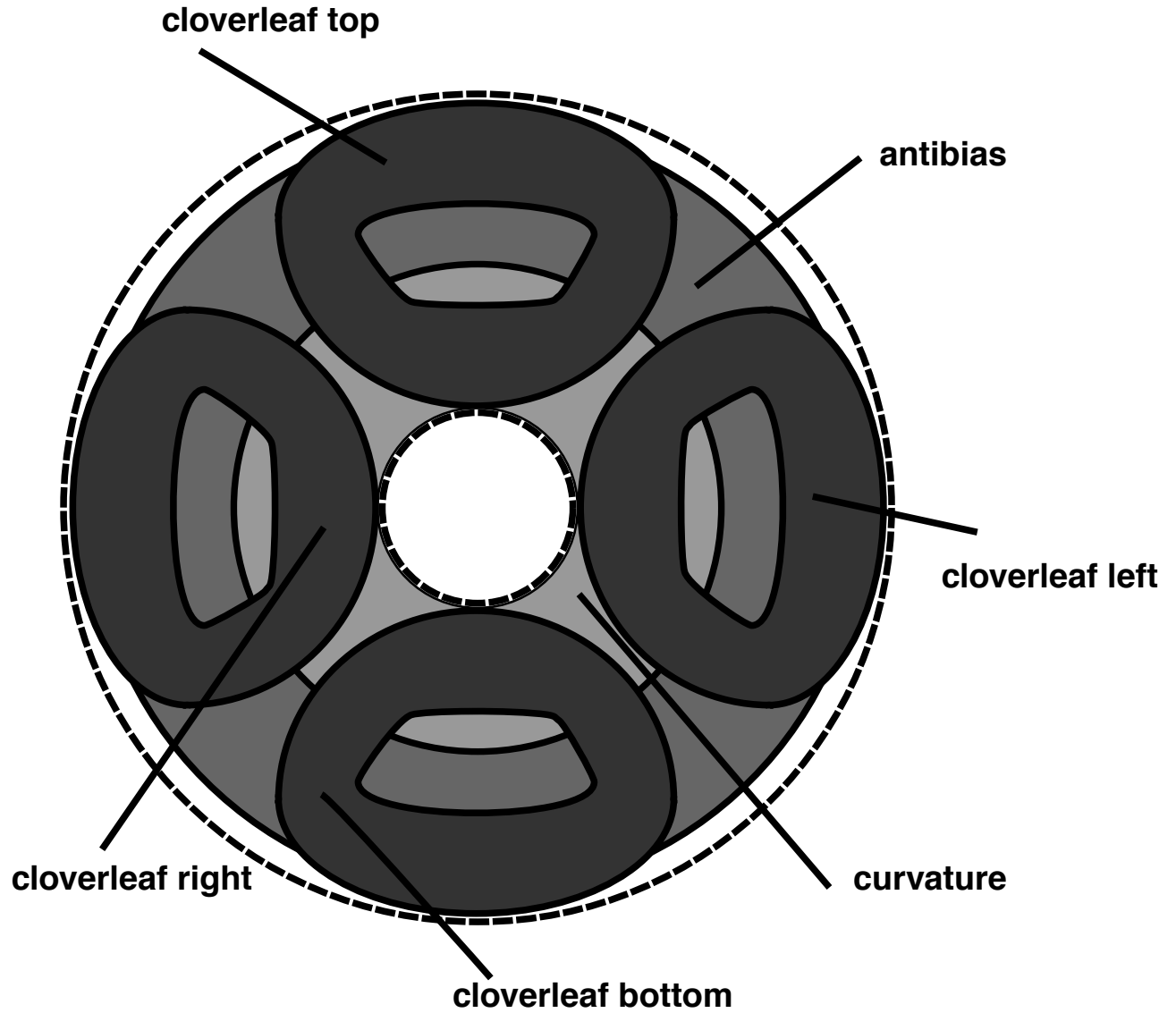


**Figure A-3:** The drawing (to scale) shows the cloverleaf coils and the "back" layer of curvature and antibias coils. The outer radius of the vacuum flange, and the clearance hole for the bucket window are indicated.





# Appendix B

## Electric connections of the trap

There are eighteen wires (labelled 1 to 18) extending from each side of the trap, which consist of nine coils each. For each side the four cloverleaf coils are labelled *top*, *down*, *right* and *left*. The antibias and curvature coils are labelled *antibias front*, *antibias back*, *curvature front*, and *curvature back*. The label *front* and *back* indicates, whether the layer of the coil is the one closer or further away from the atoms. Corresponding to their location, the two sides of the trap are labelled *Science Chamber (SC)* and *Laser Room (Laser)*.

In the following tables and figures the electrical connections of the trap are summarized and illustrated. Tables B.1 and B.2 relate the number of a wire to the corresponding coil. They give the direction of the water flow and indicate whether a thermocouple (TC) is attached to the lead. Furthermore the current directions are given for normal trap operation during evaporation.

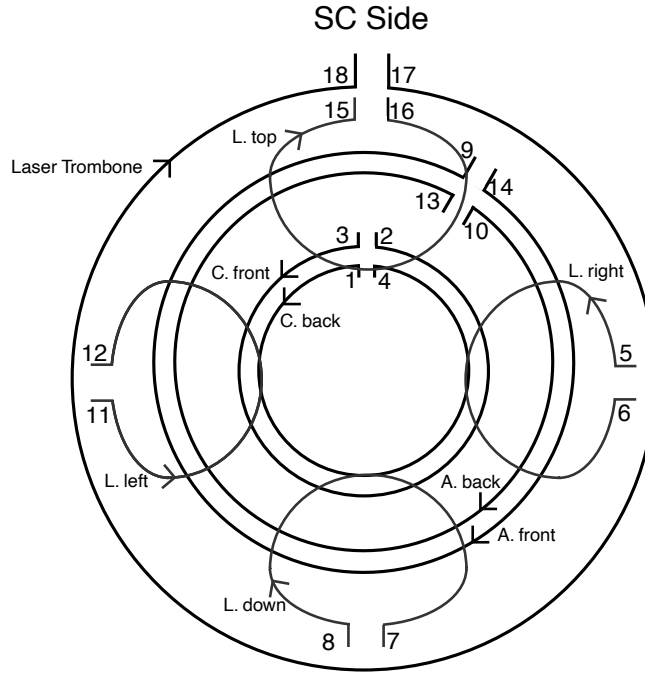
Figures B-1 and B-2 show the sense of the currents in the coils as seen by looking towards the atoms onto the backplate of each side of the trap.

The current distribution panel is shown in figure B-3. For each lug the numbers of the connected leads are given. The ports used for connecting the coils to power supplies etc. are labelled in roman numbers. Tables B.3 and B.4 show the connections made between these ports and/or power supplies etc.. In this tables G+ and G- give the positive and negative outputs of the gradient power supply unit (including IGBTs and diodes). Ditto for the MOT (MOT-,MOT+), Curvature (C+,C-), Feshbach (FA+,FA-), the two slower (S1+,S1-,S2+,S2-), and the bias (B-) power supplies. Diode+, Diode- refer to the high current diode installed in the circuit in between the curvature and antibias coils.

Figure B-4 should help to identify the leads as they leave the bucket ports.

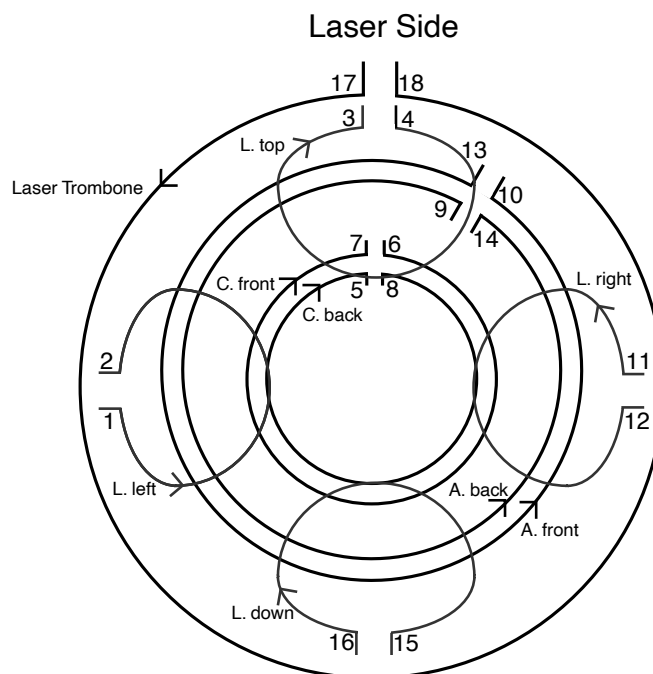
Finally, figure B-5 shows the electronic circuit for the whole trap and the slower as used in the current experiments.

| Wire | Coil             | Water | TC | Current |
|------|------------------|-------|----|---------|
| 1    | curvature back   | IN    |    | +       |
| 2    | curvature front  | OUT   | X  | -       |
| 3    | curvature front  | IN    |    | +       |
| 4    | curvature back   | OUT   | X  | -       |
| 5    | cloverleaf right | OUT   | X  | +       |
| 6    | cloverleaf right | IN    |    | -       |
| 7    | cloverleaf down  | OUT   | X  | -       |
| 8    | cloverleaf down  | IN    |    | +       |
| 9    | antibias front   | OUT   | X  | -       |
| 10   | antibias back    | IN    |    | +       |
| 11   | cloverleaf left  | OUT   | X  | +       |
| 12   | cloverleaf left  | IN    |    | -       |
| 13   | antibias back    | OUT   | X  | -       |
| 14   | antibias front   | IN    |    | +       |
| 15   | cloverleaf top   | OUT   | X  | -       |
| 16   | cloverleaf top   | IN    |    | +       |
| 17   | SC trombone      | IN    |    | +       |
| 18   | SC trombone      | OUT   |    | -       |

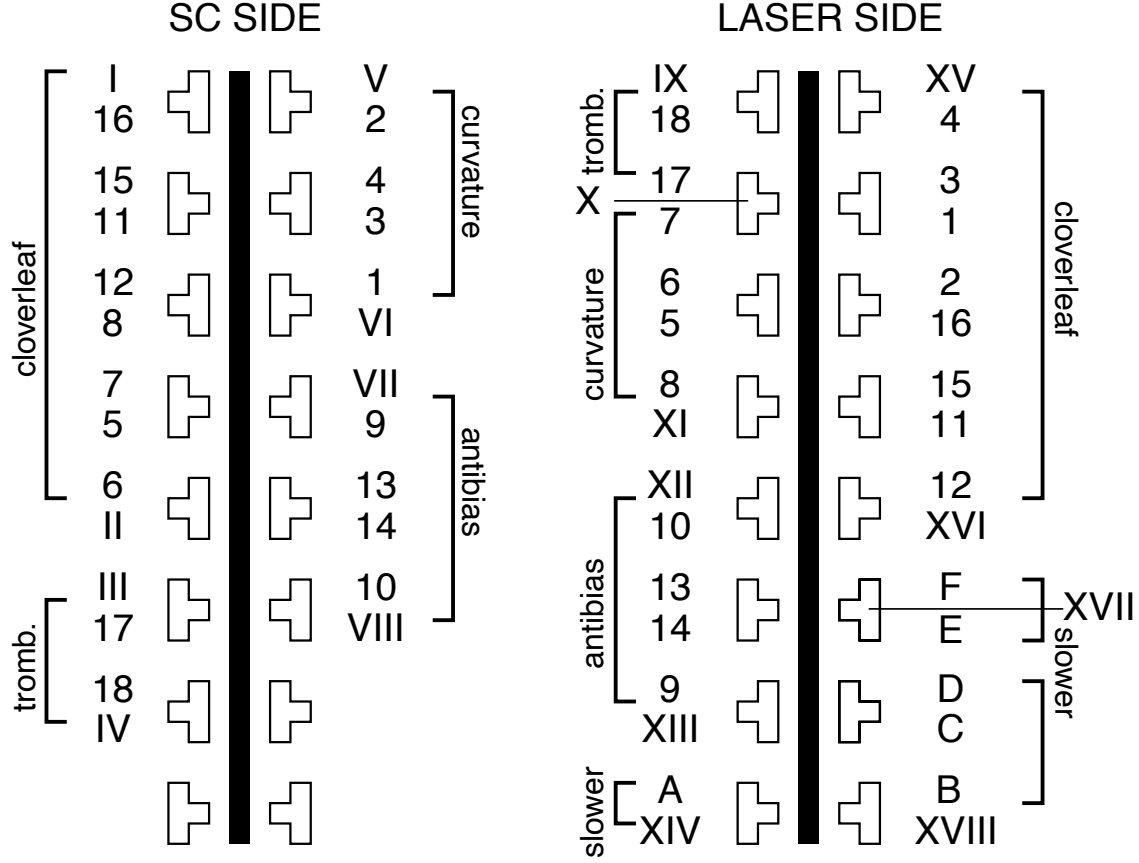
Table B.1: *Science chamber side.*Figure B-1: *Current directions science chamber side.*

| Wire | Coil             | Water | TC | Current |
|------|------------------|-------|----|---------|
| 1    | cloverleaf left  | OUT   | X  | +       |
| 2    | cloverleaf left  | IN    |    | -       |
| 3    | cloverleaf top   | OUT   | X  | -       |
| 4    | cloverleaf top   | IN    |    | +       |
| 5    | curvature back   | IN    |    | -       |
| 6    | curvature front  | OUT   | X  | +       |
| 7    | curvature front  | IN    |    | -       |
| 8    | curvature back   | OUT   | X  | +       |
| 9    | antibias back    | IN    |    | +       |
| 10   | antibias front   | OUT   | X  | -       |
| 11   | cloverleaf right | OUT   | X  | +       |
| 12   | cloverleaf right | IN    |    | -       |
| 13   | antibias front   | IN    |    | +       |
| 14   | antibias back    | OUT   | X  | -       |
| 15   | cloverleaf down  | OUT   | X  | -       |
| 16   | cloverleaf down  | IN    |    | +       |
| 17   | Laser trombone   | IN    |    | +       |
| 18   | Laser trombone   | OUT   |    | -       |

**Table B.2:** *Laser room side*



**Figure B-2:** *Current directions laser room side.*

Figure B-3: *Current panel.*

| lug        | I  | II | III | IV | V       | VI     | VII  | VIII   |
|------------|----|----|-----|----|---------|--------|------|--------|
| connection | G+ | XV | C-  | IX | XI,MOT- | Diode- | XIII | C+,FA- |

Table B.3: *External connections science chamber side.*

| lug        | IX | X  | XI | XII        | XIII     | XIV | XV | XVI | XVII    | XVIII |
|------------|----|----|----|------------|----------|-----|----|-----|---------|-------|
| connection | IV | B- | V  | Diode+,FA+ | VI, MOT+ | S2+ | II | G-  | S2-,S1- | S1+   |

Table B.4: *External connections laser room side.*

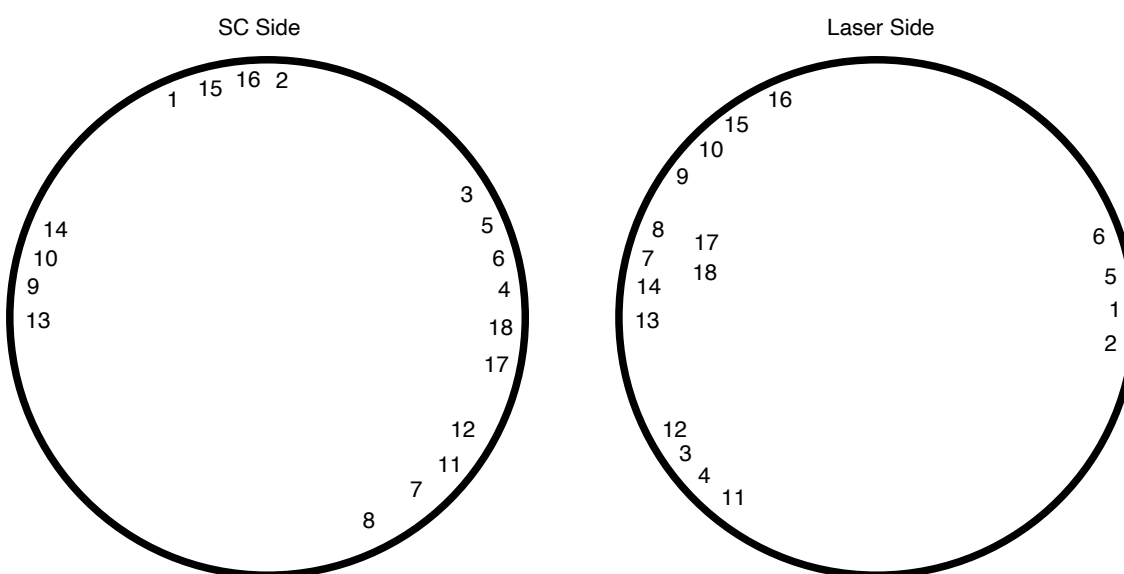


**Figure B-4:** *The position of the leads at the bucket ports.*

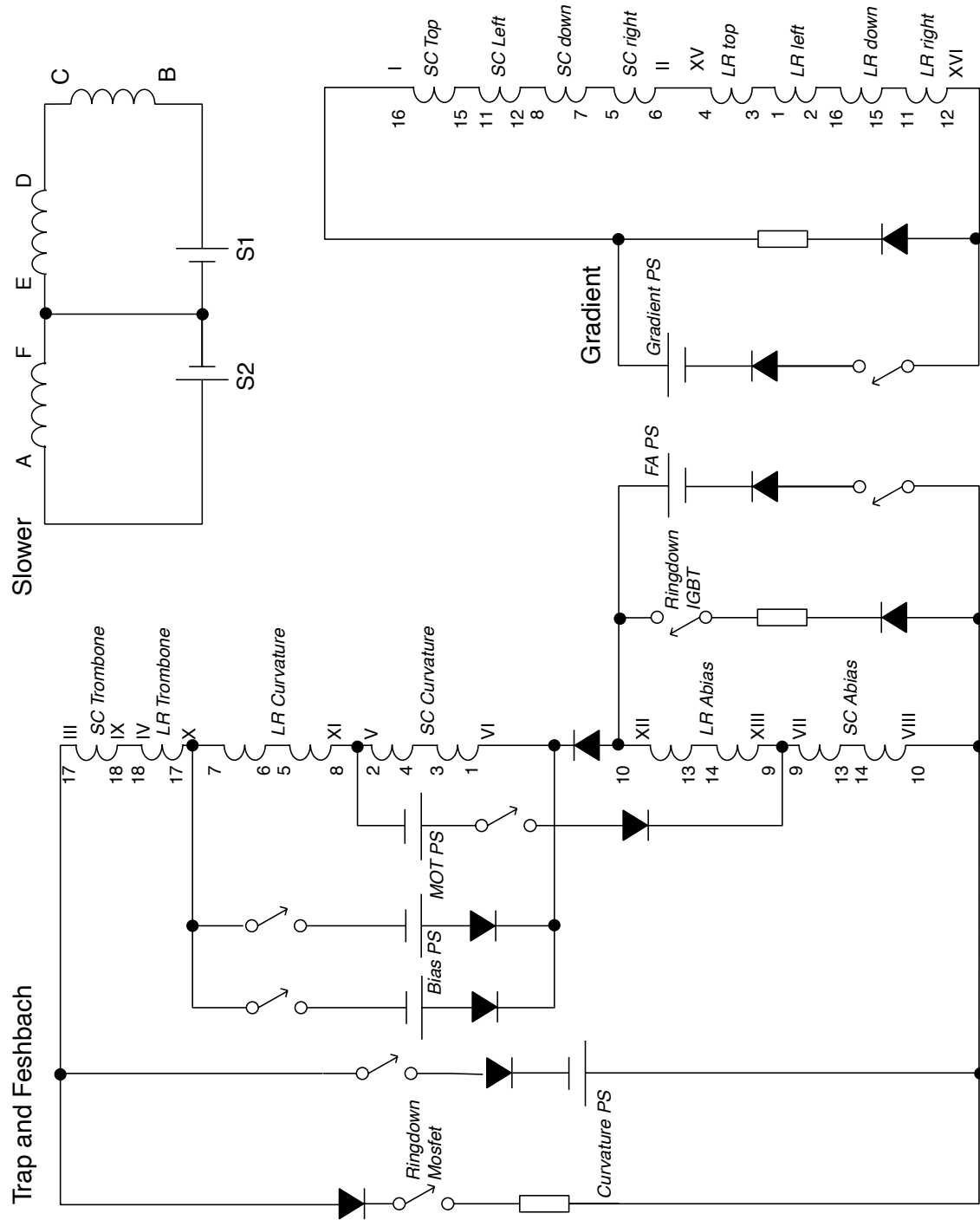


Figure B-5: Electric circuit for the operation of trap and the slower

# Appendix C

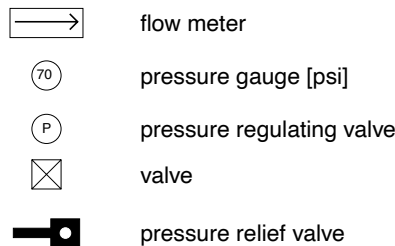
## Water distribution panel

Figure C-2 shows the distribution panel for the cooling water. The symbols employed are explained in figure C-1. The top quarter of the panel is used for the low pressure water circuit. It consists of one input manifold and three smaller return manifolds. Via the input manifold the water is distributed to high power diodes and IGBT's as well as the cold plate in the oven region of the vacuum chamber. The flow of the returning water is monitored by flow meters at the end of the low pressure return manifolds and can be adjusted via pressure regulating valves. The water is finally collected in the vertical return manifold.

Each side of the magnetic trap has a separate high pressure input manifold. The water returning from the trap is collected in twelve return manifolds. The exits (inputs) of the input (return) manifolds are labelled with the number of the lead of the trap they are connected to. As in the low pressure circuit the flows are monitored by flow meters before the water is collected in the vertical return manifold.

The flow meters provide a voltage proportional to the measured flow that is read out by the 2700 Keithley multimeter (see chapter 4.3). The flow meters are numbered by the corresponding channels of this device. For an easier orientation, the name of the flow monitored coils or electronic devices is given next to the flow meter symbols.

To protect the flow meters, the return lines have pressure relieve valves that open if a pressure of 75 psi is exceeded. The released water is collected via safety return manifolds.



**Figure C-1:** Symbols in figure C-2. The numbers in the pressures gauges indicate typical operating pressures.

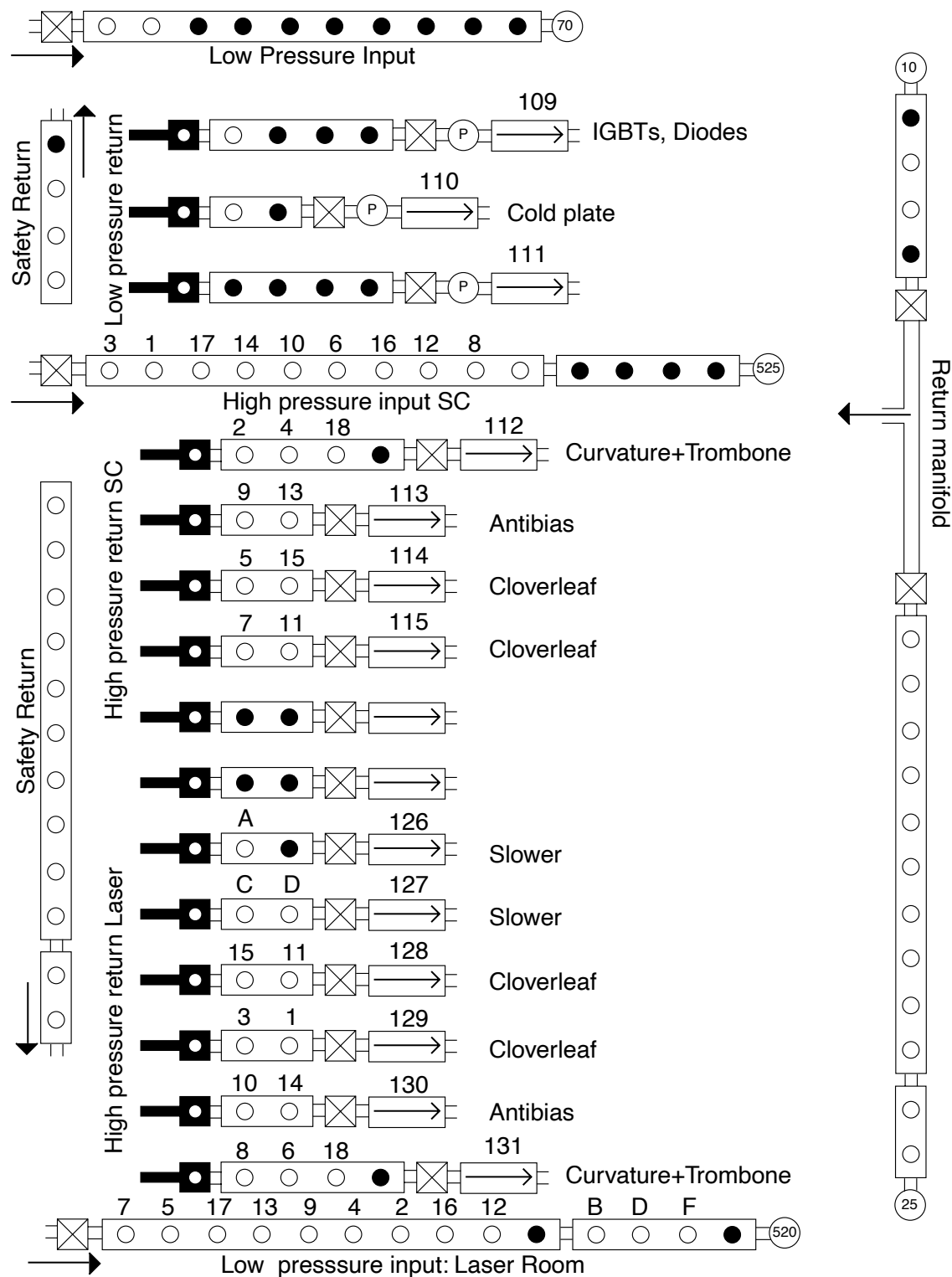


Figure C-2: Water distribution panel



# Bibliography

- [1] M.H. Anderson *et al.*, *Science* **269**, 198 (1995); K.B. Davis *et al.*, *Phys. Rev. Lett.* **75**, 3969 (1995); C.C. Bradley *et al.*, *Phys. Rev. Lett.* **75**, 1687 (1995); C. C. Bradley *et al.*, *Phys. Rev. Lett.* **78**, 985 (1997); D. G. Fried *et al.*, *Phys. Rev. Lett.* **81**, 3811 (1998); A. Robert *et al.*, *Science* **292**, 461 (2001); F. Pereira Dos Santos *et al.*, *Phys. Rev. Lett.* **86**, 3459 (2001); G. Modugno *et al.*, *Science* **297**, 2240 (2002)
- [2] For a review see: J. Anglin and W. Ketterle. Bose-Einstein condensation of atomic gases. *Nature*, **416**, 211 (2002)
- [3] S. Inouye, M.R. Andrews, J. Stenger, H.-J. Miesner, D.M. Stamper-Kurn and W. Ketterle. Observation of Feshbach resonances in a Bose-Einstein condensate. *Nature* **392**, 151, (1998)
- [4] B. DeMarco and D.S. Jin. Onset of Fermi Degeneracy in a Trapped Atomic Gas. *Science* **285**, 1703 (1999)
- [5] B. DeMarco and D.S. Jin. Exploring a quantum degenerate gas of fermionic atoms. *Phys. Rev. A* **58**, R4267 (1998)
- [6] B. DeMarco, J. L. Bohn, J. P. Burke, Jr., M. Holland, and D. S. Jin. Measurement of p-Wave Threshold Law Using Evaporatively Cooled Fermionic Atoms. *Phys. Rev. Lett.* **82**, 4208 (1998)
- [7] B. DeMarco, S.B. Papp, and D.S. Jin. Pauli Blocking of Collisions in a Quantum Degenerate Atomic Fermi Gas. *Phys. Rev. Lett.* **86**, 24, 5409 (2001)
- [8] S. D. Gensemer and D. S. Jin. Transition from Collisionless to Hydrodynamic Behavior in an Ultracold Fermi Gas. *Phys. Rev. Lett.* **87**, 173201 (2001)
- [9] B. DeMarco and D.S. Jin. Spin Excitations in a Fermi Gas of Atoms. *Phys. Rev. Lett.* **88**, 040405 (2002)
- [10] T. Loftus, C. A. Regal, C. Ticknor, J. L. Bohn, and D. S. Jin. Resonant Control of Elastic Collisions in an Optically Trapped Fermi Gas of Atoms. *Phys. Rev. Lett.* **88**, 173201 (2002)

- 
- [11] C.A. Regal, C. Ticknor, J.L. Bohn, D.S. Jin. Tuning p-wave interactions in an ultracold Fermi gas of atoms. cond-mat/0209071 (2002)
  - [12] Andrew G. Truscott, K.E. Strecker, W.I. McAlexander, G.B. Partidge, and R.G.Hulet. Observation of Fermi Pressure in a Gas of Trapped Atoms. *Science* **291**, 2570 (2001)
  - [13] F. Schreck, L. Khaykovich, K. L. Corwin, G. Ferrari, T. Bourdel, J. Cubizolles, and C. Salomon. Quasipure Bose-Einstein Condensate Immersed in a Fermi Sea. *Phys. Rev. Lett.*, **87**, 080403 (2001)
  - [14] C. A. Sackett, J. M. Gerton, M. Welling, and R. G. Hulet. Measurements of Collective Collapse in a Bose-Einstein Condensate with Attractive Interactions. *Phys. Rev. Lett.* **82**, 876 (1999)
  - [15] Z.Hadzibabic, C.A.Stan, K.Dieckmann, S.Gupta, M.W.Zwierlein, A.Goerlitz, and W.Ketterle *Phys. Rev. Lett.* **88**, 160401 (2002)
  - [16] K. Dieckmann, C. A. Stan, S. Gupta, Z. Hadzibabic, C. H. Schunck, and W. Ketterle. Decay of an ultracold fermionic lithium gas near a Feshbach resonance. *Phys. Rev. Lett.* **89**, 203201 (2002)
  - [17] S. Jochim, M. Bartenstein, G. Hendl, J. Hecker Denschlag, R. Grimm, A. Mosk, M. Weidemüller. Magnetic field control of elastic scattering in a cold gas of fermionic lithium atoms. physics/0207098 (2002)
  - [18] S. R. Granade, M. E. Gehm, K. M. O'Hara, and J. E. Thomas. All-Optical Production of a Degenerate Fermi Gas. *Phys. Rev. Lett.* **88**, 120405 (2002)
  - [19] K.M. O'Hara, S.L. Hemmer, S.R. Granade, M.E. Gehm, J.E. Thomas, V.Venturi, E. Tiesinga, C.J. Williams. Measurement of the Zero Crossing in a Feshbach Resonance of Fermionic 6-Li. *Phys. Rev. A* **66**, 041401 (2002)
  - [20] K.M. O'Hara, S.L. Hemmer, M.E. Gehm, S.R. Granade, J.E. Thomas. Observation of a Strongly Interacting Degenerate Fermi Gas of Atoms. Science Express 10.1126/science.1079107
  - [21] G. Roati, F. Riboli, G. Modugno, and M. Inguscio. Fermi-Bose Quantum Degenerate K - Rb Mixture with Attractive Interaction. *Phys. Rev. Lett.* **89**, 150403 (2002)
  - [22] G. Ferrari, M. Inguscio, W. Jastrzebski, G. Modugno, G. Roati, and A. Simoni. Collisional Properties of Ultracold K-Rb Mixtures. *Phys. Rev. Lett.* **89**, 053202 (2002)
  - [23] Giovanni Modugno, Giacomo Roati, Francesco Riboli, Francesca Ferlaino, Robert J. Brecha, and Massimo Inguscio. Collapse of a Degenerate Fermi Gas. *Science* **297**, 2240 (2002)

- [24] J. Stenger, S. Inouye, M. R. Andrews, H.-J. Miesner, D. M. Stamper-Kurn, and W. Ketterle. Strongly Enhanced Inelastic Collisions in a Bose-Einstein Condensate near Feshbach Resonances. *Physical Review Letters* **82**, 2422 (1999)
- [25] H.A.Feshbach. A unified theory of nuclear reactions. II *Ann. Phys.* **19**, 287 (1962)
- [26] E.R.I. Abraham, W.I. McAlexander, J.M. Gerton, R.G. Hulet, R. Côté and A. Dalgarno. Triplet s-wave resonance in  $^6\text{Li}$  collisions and scattering lengths of  $^6\text{Li}$  and  $^7\text{Li}$ . *Phys. Rev. A* **55**, R3299 (1997)
- [27] M. Houbiers, H.T.C. Stoof, W.I. McAlexander, and R.G. Hulet. Elastic and inelastic collisions of  $^6\text{Li}$  atoms in magnetic and optical traps. *Phys. Rev. A* **57**, R1497 (1997)
- [28] H. T. C. Stoof, M. Houbiers, C. A. Sackett, and R. G. Hulet. Superfluidity of Spin-Polarized  $^6\text{Li}$ . *Phys. Rev. Lett.* **76**, 10 (1996)
- [29] M. Houbiers, R. Ferwerda, H. T. C. Stoof, W. I. McAlexander, C. A. Sackett, and R. G. Hulet. Superfluid state of atomic  $^6\text{Li}$  in a magnetic trap. *Phys. Rev. A* **56**, 4864 (1997)
- [30] R. Combescot. Trapped  $^6\text{Li}$ : A High  $T_c$  Superfluid? *Phys. Rev. Lett.*, **83** 3766 (1999)
- [31] M. Houbiers and H. T. C. Stoof. Cooper-pair formation in trapped atomic Fermi gases. *Physical Review A*, **59**, 1556 (1999)
- [32] A.J.Legget. *Journal de Physique* **41**, C7 (1980)
- [33] M. A. Baranov and D. S. Petrov . Critical temperature and Ginzburg-Landau equation for a trapped Fermi gas. *Phys. Rev. A* **58** R801 (1998)
- [34] M.J. Holland, S.J.J.M.F. Kokkelmans, M.L. Chiofalo, and R. Walser. Resonance Superfluidity in a Quantum Degenerate Fermi Gas. *Phys. Rev. Lett.* **87**, 120406 (2001)
- [35] E. Timmermans, K. Furuya, P.W. Milonni, and A.K. Kerman, *Phys. Rev. A*. **285**, 228 (2001)
- [36] E. Timmermans. Degenerate Fermion Gas Heating by Hole Creation. *Phys. Rev. Lett.* **87**, 240403 (2001)
- [37] Y. Ohashi and A. Griffin. BCS-BEC Crossover in a Gas of Fermi Atoms with a Feshbach Resonance. *Phys. Rev. Lett.* **89**, 130402 (2002)

- [38] J. N. Milstein, S. J. J. M. F. Kokkelmans, and M. J. Holland. Resonance theory of the crossover from Bardeen-Cooper-Schrieffer superfluidity to Bose-Einstein condensation in a dilute Fermi gas. *Phys. Rev. A* **66**, 043604 (2002)
- [39] D.S. Petrov. Three-body problem in Fermi gases with short-range interparticle interaction. cond-mat/0209246
- [40] W. Hofstetter, J. I. Cirac, P. Zoller, E. Demler, and M. D. Lukin. High-Temperature Superfluidity of Fermionic Atoms in Optical Lattices *Phys. Rev. Lett.* **89**, 220407 (2002)
- [41] C. R. Monroe, E. A. Cornell, C. A. Sackett, C. J. Myatt, and C. E. Wieman. Measurement of Cs-Cs elastic scattering at  $T=30\ \mu\text{K}$ . *Phys. Rev. Lett.* **70**, 414 (1993)
- [42] M.O. Mewes, M.R. Andrews, N.J. van Druten, D.M. Kurn, D.S. Durfee, and W. Ketterle, *Phys. Rev. Lett.* **77**, 416 (1996).
- [43] D.M. Stamper-Kurn, Ph.D. thesis, Massachusetts Institute of Technology, (2000)
- [44] M.O. Mewes, Ph.D thesis, Massachusetts Institute of Technology, (1997)
- [45] O.J. Luiten, Ph.D. thesis, University of Amsterdam, (1993)
- [46] M. Zwierlein, Massachusetts Institute of Technology (2001)
- [47] Z. Hadzibabic, Massachusetts Institute of Technology, 2001
- [48] U. Schünemann, H. Engler, M. Zielonkowski, M. Weidemüller, R. Grimm. Magneto-optic trapping of lithium using semiconductor lasers. *Optics Comm.* **158**, 263 (1998)
- [49] W. Phillips and H. Metcalf. Laser Deceleration of an Atomic Beam. *Phys. Rev. Lett.* **48**, 596 (1982).
- [50] E.L. Raab, M. Prentiss, A. Cable, S. Chu, and D.E. Pritchard. Trapping of Neutral Sodium Atoms with Radiation Pressure. *Phys. Rev. Lett.* **59**, 23, 2631-2634 (1987)
- [51] J. Dalibard et C. Cohen-Tannoudji. Laser Cooling Below the Doppler Limit by Polarization Gradients – Simple Theoretical Models. *J. Opt. Soc. Am. B* **6**, 2023-2045 (1989)
- [52] P.J. Ungar, D.S. Weiss, E. Riis, S. Chu. Optical molasses and ultracold atoms: theory. *J. Opt. Soc. Am. B* **6**, 2058-71 (1989)

- 
- [53] S. Chu, L. Hollberg, J. Bjorkholm, A. Cable, and A. Ashkin. Three-Dimensional Viscous Confinement and Cooling of Atoms by Resonance Radiation Pressure. *Phys. Rev. Lett.* **55**, 48 (1985)
- [54] D.J. Wineland, W.M. Itano. Laser Cooling of Atoms. *Phys. Rev. A* **20**, 1521 (1979)
- [55] P.D. Lett, R.N. Watts, C.I. Westbrook, and W.D. Phillips. Observation of Atoms Laser Cooled below the Doppler Limit. *Phys. Rev. Lett.* **61**, 169 (1988)
- [56] D.E. Pritchard. Cooling Neutral Atoms in a Magnetic Trap for Precision Spectroscopy. *Phys. Rev. Lett.* **51**, 1336 (1983)
- [57] W.H. Wing. On neutral particle trapping in quasistatic electromagnetic fields. *Prog. Quant. Electr.* **8**, 181 (1984)
- [58] Y.V. Gott, M.S. Ioffe, and V.G. Tel'kovskii. *Nuclear Fusion Supplement* **3**, 1045 (1962)
- [59] H.F. Hess, G.P. Kochansky, J.M. Doyle, N. Masuhara, D. Kleppner, and T.J. Greytak. Magnetic Trapping of Spin-Polarized Atomic Hydrogen. *Phys. Rev. Lett.* **59**, 672 (1987)
- [60] O.J. Luiten, M.W. Reynolds, and J.T. Walraven, "Kinetic Theory of the evaporative Cooling of a trapped Gas", *Physical Review A*, **53**, 381 (1996)
- [61] G. Breit and I.I. Rabi. Measurement of nuclear spin. *Physical Review* **38**, 2082 (1931)
- [62] W. Ketterle and N.J. van Druten. Evaporative cooling of trapped atoms. *Advances in Atomic, Molecular, and Optical Physics*, **37**, 181 (1996)
- [63] R. Grimm, M. Weidemüller, and Y.B. Ovchinnikov. Optical Dipole Traps For Neutral Atoms. *Advances in Atomic, Molecular, and Optical Physics*, **42**, 95 (2000)
- [64] W. Ketterle, D.S. Durfee and D.M. Stamper-Kurn, in Proceedings of the International School of Physics "Enrico Fermi", *Bose Einstein condensation in Atomic Gases*, M. Inguscio, S. Stringari, and C. Wieman Eds. (IOS Press, Amsterdam 1999)
- [65] S.J.J.M.F. Kokkelmans and E. Tiesinga (private communication).
- [66] C. Cohen-Tannoudji, J. Dupont-Roc, G. Grynberg. Atom-Photon Interactions. *Wiley Science, New York* (1998)
- [67] S. Chu. Manipulating of neutral particles. *Rev. Mod. Phys.* **70**, 685 (1998)

- [68] W.D. Phillips. Laser Cooling and trapping of neutral atoms. *Rev. Mod. Phys.* **70** 721 (1998)
- [69] C. Cohen-Tannoudji. Manipulating Atoms with Photons. *Rev. Mod. Phys.* **70** 707 (1998)
- [70] W. Ketterle, D.S. Durfee, and D.M. Stamper-Kurn. Making, Probing and understanding Bose-Einstein condensates. In M. Inguscio, S.Stringari and C.E.Wieman eds., *Bose-Einstein Condensation in Atomic Gases*, Proceedings of the "Enrico Fermi" Summer School, July 1998, Varenna, Italy.
- [71] J. Dalibard. Collisional dynamics of ultra-cold atomic gases. In M. Inguscio, S.Stringari and C.E.Wieman eds., *Bose-Einstein Condensation in Atomic Gases*, Proceedings of the "Enrico Fermi" Summer School, July 1998, Varenna, Italy.

## ERKLÄRUNG:

Ich versichere, diese Arbeit selbständig verfaßt und keine anderen als die angegebenen Quellen und Hilfsmittel benutzt zu haben.

Heidelberg, den 1. Dezember 2002